Molecular Cancer

RESEARCH

Open Access

Targeting circ-0034880-enriched tumor extracellular vesicles to impede SPP1^{high}CD206^{+} pro-tumor macrophages mediated pre-metastatic niche formation in colorectal cancer liver metastasis

Jing Zhou[1,2†], Qing Song[3†], Haoze Li[1†], Yicun Han[1], Yunzhou Pu[1], Ling Li[1], Wenqing Rong[1], Xiaodie Liu[1], Ziyuan Wang[4], Jian Sun[5], Yuqing Song[6], Xueyan Hu[6], Guanghao Zhu[6], Huirong Zhu[1], Liu Yang[7*], Guangbo Ge[6*], Hongshan Li[2*] and Qing Ji[1*]

Abstract

Background Information transmission between primary tumor cells and immunocytes or stromal cells in distal organs is a critical factor in the formation of pre-metastatic niche (PMN). Understanding this mechanism is essential for developing effective therapeutic strategy against tumor metastasis. Our study aims to prove the hypothesis that circ-0034880-enriched tumor-derived extracellular vesicles (TEVs) mediate the formation of PMN and colorectal cancer liver metastasis (CRLM), and targeting circ-0034880-enriched TEVs might be an effective therapeutic strategy against PMN formation and CRLM.

Methods We utilized qPCR and FISH to measure circRNAs expression levels in human CRC plasma, primary CRC tissues, and liver metastatic tissues. Additionally, we employed immunofluorescence, RNA sequencing, and *in vivo* experiments to assess the effect mechanism of circ-0034880-enriched TEVs on PMN formation and CRC metastasis. DARTS, CETSA and computational docking modeling were applied to explore the pharmacological effects of Ginsenoside Rb1 in impeding PMN formation.

Results We found that circ-0034880 was highly enriched in plasma extracellular vesicles (EVs) derived from CRC patients and closely associated with CRLM. Functionally, circ-0034880-enriched TEVs entered the liver tissues and were absorbed by macrophages in the liver through bloodstream. Mechanically, TEVs-released circ-0034880 enhanced the activation of SPP1^{high}CD206^{+} pro-tumor macrophages, reshaping the metastasis-supportive host

† Jing Zhou, Qing Song and Haoze Li contributed equally to this work.

*Correspondence:
Liu Yang
bsyykyc@shutcm.edu.cn
Guangbo Ge
geguangbo@shutcm.edu.cn
Hongshan Li
lihongshan_1982@126.com
Qing Ji
ttt99118@hotmail.com
Full list of author information is available at the end of the article

stromal microenvironment and promoting overt metastasis. Importantly, our mechanistic findings led us to discover that the natural product Ginsenoside Rb1 impeded the activation of SPP1^{high}CD206^{+} pro-tumor macrophages by reducing circ-0034880 biogenesis, thereby suppressing PMN formation and inhibiting CRLM.

Conclusions Circ-0034880-enriched TEVs facilitate strong interaction between primary tumor cells and SPP1^{high}CD206^{+} pro-tumor macrophages, promoting PMN formation and CRLM. These findings suggest the potential of using Ginsenoside Rb1 as an alternative therapeutic agent to reshape PMN formation and prevent CRLM.

Keywords Tumor metastasis, Pro-tumor macrophages, Extracellular vesicles, Circ-0034880, Ginsenoside Rb1

Background

Colorectal cancer (CRC) is a prevalent malignant tumor, ranking third in terms of incidence rate and second in mortality rate worldwide [1, 2]. Treatment modalities such as surgery, radiotherapy, chemotherapy, molecular targeted therapy, and immunotherapy have significantly enhanced the survival rate among CRC patients [3]. Nevertheless, despite frequent follow-up, approximately 19.4–20.1% of CRC patients still experience tumor recurrence and distal organ metastasis post-surgery [4]. Consequently, postoperative recurrence and metastasis have emerged as leading causes of death in CRC patients [5], with liver metastasis posing a significant obstacle to their long-term survival [3]. Thus, there is a critical need to delve deeply into the pathological and molecular mechanisms underlying liver metastasis, overcome existing treatment barriers post-surgery, and explore more effective therapeutic strategies to improve the survival rate of postoperative CRC patients.

Numerous studies have elucidated the underlying pathological and molecular mechanisms governing the relationship between primary tumors and distal organ metastasis [6–8]. Increasing evidence highlights the significance of pre-metastatic niche (PMN) formation, which substantially contributes to the metastasis-supportive tumor microenvironment (TME) prior to the arrival and colonization of disseminated tumor cells [9]. Extracellular vesicles (EVs), as functional entities secreted by various cells, are replete with proteins, nucleic acids, lipids, and other molecules, facilitating crucial communication between tumor cells and stromal cells. This communication reshapes the TME and provides essential support for the establishment and growth of metastatic tumor cells [10]. An increasing number of reports suggest that tumor-derived EVs (TEVs) contribute to the formation of PMN, providing essential TME for the proliferation of circulating tumor cells in metastatic organs [11, 12]. As an organ with abundant macrophages, the activation of pro-tumor macrophages in the liver contributes to the formation of PMN and the remodeling of TME, ultimately leading to the metastasis and growth of tumor cells [13, 14]. Circular RNAs (circRNAs) have emerged as a large class of primarily non-coding RNAs, many of which are abundantly enriched in tumor patients' blood, cells, tissues and EVs, and have crucial roles in tumor development and progression through diverse biological mechanisms. Here, we aim to prove our hypothesis that circ-0034880-enriched TEVs mediate the formation of PMN and CRLM, and targeting circ-0034880-enriched TEVs might be an effective therapeutic strategy against PMN formation and CRLM.

In our study, we demonstrated a close association between circ-0034880-enriched TEVs from the plasma of CRC patients and CRLM. Our mechanistic investigation revealed that circ-0034880-enriched TEVs can reshape the TME by activating SPP1^{high}CD206^{+} pro-tumor macrophages within liver tissues. Furthermore, our mechanistic findings led us to discover that the natural product Ginsenoside Rb1 impedes the activation of SPP1^{high}CD206^{+} pro-tumor macrophages by reducing circ-0034880 biogenesis, thereby suppressing PMN formation and inhibiting CRLM.

Materials and methods

Data analysis using exoRBase and GEO dataset

The differentially expressed circRNAs in the plasma EVs of CRC patients were screened using exoRBase 2.0 (http://www.exorbase.org/exoRBaseV2/) [15]. Use circBase database (http://circrna.org/) to note circRNAs [16]. Use the GEO (Gene Expression Omnibus) database to obtain the circRNA gene chip: GSE159669. Use edgeR in R software (v3.3.2) to calculate the differential expression of circRNAs. The differentially expressed circRNAs were identified by multiple change (fold change, FC ≥ 2.0, that is, |log2FC |> 1) and T test ($P < 0.05$) between CRC tissues and paracancerous tissues.

Human samples

All the human CRC plasma samples, primary CRC tissue and hepatic metastasis tissue samples were collected between 2020 and 2022 at Shuguang Hospital, Shanghai University of Traditional Chinese Medicine. The general clinical information of all enrolled 120 CRC patients was

included in Table S1. The plasma samples from healthy volunteers were used as control. All clinical tissues and plasma samples were obtained with informed consent and all protocols were approved by the Ethics Committee at Shuguang Hospital, Shanghai University of Traditional Chinese Medicine.

EVs purification and characterization

The minimal experimental requirements for the definition of EVs refer to the report by Lötvall J, et al. [17]. All the EVs used in our experiments were purified by sequential centrifugation [18]. In brief, live cells, possible apoptotic bodies and large cell debris were firstly removed from the plasma of CRC patients or cell culture medium by two step centrifugation: 500×*g* for 10 min, and 12,000×*g* for 20 min. Subsequently, the pellets containing EVs were collected by spinning at 100,000×*g* for 70 min. After washing with PBS, the pellets were deal with ultracentrifugation (Beckman 70Ti rotor). The quality, size and particle number of EVs were characterized by electron microscopy and LM10 nanoparticle characterization system (NanoSight, Malvern Instruments). All the purified EVs pellets were resuspended in PBS. The protein concentration for each EVs sample was determined by BCA (Pierce, Thermo Fisher Scientific). Normal EVs from healthy volunteers' plasma or normal human colonic epithelial cells NCM460 or murine colonic epithelial cells MODEK were simultaneously purified for the control in our studies.

Cell culture

Human CRC cell lines HCT116, Caco2, LoVo, SW480, SW620, HCT115, HT29, HCT8, human colonic epithelial cells NCM460, human THP-1 monocyte/macrophages, murine colon cancer cell lines MC38, and murine colonic epithelial cells MODEK were purchased from ATCC or Chinese Academy of Sciences Shanghai Cell Bank. HCT116, Caco2, LoVo, SW480, SW620, HCT115, HT29, HCT8, NCM460, THP-1 were cultured in RPMI1640, Dulbecco's Modified Eagle Medium (DMEM), F12-K medium, or Leibovitz's L-15 medium, respectively. MC38 and MODEK were cultured in DMEM medium. All the media were supplemented with 10% EVs-free FBS, 100 U/mL penicillin and 100 mg/mL streptomycin.

Isolation and polarization of mouse BMDMs

Primary mouse BMDMs were isolated from the femur of the C57BL/6 mice according to the publication by Zhang et al. [19]. BMDMs were plated at 1×10^6 cells per 10 cm dish (Corning Lifesciences, Tewksbury, MA, USA) with 10 mL of macrophage complete media (DMEM, 10%FBS), containing 50 ng/mL mouse recombinant macrophage colony-stimulating factor (M-CSF; Biolegend, San Diego, CA, USA) and cultured for 7 days, with the change of media and M-CSF on day 5. On day 7, the mouse BMDMs were stimulated with 50 ng/mL IL-4 (Biolegend, San Diego, CA, USA) for 48 h for the activation of $CD206^+$ pro-tumor macrophages, or co-cultured with 10 μg/mL MC38-EVs, 10 μg/ml MC38shRNA-EVs for 48 h according to our research objects.

Tumor mouse model

Female C57BL/6 mice at the age between 6-week-old and 8-week-old were obtained from SLAC (SLAC Laboratory Lab, Shanghai, China) and maintained under a 12-h dark/12-h light cycle with food and water provided ad libitum. All animals were randomly assigned to groups before experiments. The experimenter was not blind to the assignment of the groups and the evaluation of the results. No samples, animals or data, were excluded. For EVs localization, education and tumor metastatic experiments, C57BL/6 J mice between 6-week-old and 8-week-old were used. For *in vivo* EVs education administration, C57BL/6 J mice between 6-week-old and 8-week-old received 10 μg of EVs via tail vein every other day for 3 weeks. Experimental liver metastases were achieved by intra-splenic injection of a Luc-labeled MC38 single-cell suspension at 2×10^6 cells/injection site. Five to seven weeks later, prior to *in vivo* imaging, the mice were anesthetized with phenobarbital sodium, and established liver metastases images were observed by LB983 NIGHTOWL II system. Finally, the mice were anesthetized with phenobarbital sodium, the liver organs were excised, and the metastatic lesions were determined by HE staining. All the experimental procedures involving mice were carried out as prescribed by the National Guidelines for Animal Usage in Research (China) and were approved by the Ethics Committee at Shanghai University of Traditional Chinese Medicine.

Tissue immunofluorescence staining

For histological analysis, the dissected tissues were fixed in a mixture of 2% PFA and 20% sucrose solution for 24 h at room temperature, and then embedded in Tissuetek O.C.T. (Electron Microscopy Sciences). Blocks were frozen in a dry ice and ethanol bath. For immunofluorescence, 6 μm O.C.T. tissue cryosections were stained with antibodies against α-SMA (ab5694, Abcam, 1: 200), CD11B (ab133357, Abcam, 1: 4,000), Ly6G (ab238132, Abcam, 1: 1,000), CD3 (ab133357, Abcam, 1: 100), CD206 (24595, CST, 1: 400), F4/80 (#30325, CST, 1: 800), CD86 (#91882, CST, 1: 800), SPP1 (#88742, CST, 1: 800). Secondary antibodies conjugated to Alexa Fluor® 488 conjugated-anti-rabbit IgG (H + L) (#4412, CST, 1: 2,000) and Alexa Fluor® 594 conjugated-goat anti-rabbit IgG (#8889, CST, 1: 2,000) were used. Nuclear staining

was done with DAPI (40, 6-diamidino-2-phenylindole). Immunofluorescence images were taken with a TCS SP8 STED 3X ultra-high resolution confocal system (Leica, Ernst-Leitz, Wetzlar, Germany).

Drug affinity responsive target stability

The DATRS experiment was performed according to the protocols provided by Lomenick et al. [20]. Briefly, MC38 cells were plated in 10 cm^2 culture dishes and grown until 80% confluent. According to the manufacturer's protocol, using mammalian protein extraction reagent (M-PER) supplemented with protease and phosphatase inhibitors for protein extraction. After centrifuging the lysates at 14,000 rpm for 15 min, the supernatant was collected. Ginsenoside Rb1 (5 mg) or DMSO control was mixed with the supernatants and incubated for 30 min. The mixture was proteolyzed using protease, in which case the protein bound to the drug becomes more resistant to protease hydrolysis. All the steps were performed on ice to help prevent premature protein degradation. Gel bands were cut out and prepared for mass spectrometry analysis with trypsin digestion. Peptides were analyzed by LC/MS/MS on a Thermo LTQ-Orbitrap mass spectrometer. For quantitative comparison of protein and peptide abundances, MS spectra were analyzed by using the differential workflow of Rosetta Elucidator (Rosetta Inpharmatics) [21].

Molecular docking simulations

The 3D structures of PHAX (Q9JJT9), HNRPLL (Q921F4), QKI (Q9QYS9), and EIF4G1 (Q6NZJ6) were obtained from the Alphafold Protein Structure Database for docking simulations [22]. The structures were submitted to CavityPlus 2022 with loose loops deleted to obtain reliable prediction of binding pockets [23]. Docking simulations were conducted using Ginsenoside Rb1 (PubChem CID 9898279) and AutoDock Vina 1.2.3 in AutoDockTools 1.5.7 to assess binding affinities and optimal poses [24]. Dock preparation encompassed tasks such as hydrogen addition and Gasteiger charge assignment. The grid boxes were defined based on the predicted binding pockets of proteins, spanning approximately 22.5 Å in each direction. The default settings were maintained for the number of binding modes, exhaustiveness, and maximum energy difference (kcal/mol). The docked poses of Ginsenoside Rb1 onto PHAX, HNRPLL and EIF4G1 with the highest scores were collected for protein–ligand interaction analysis, and the docked pose of Ginsenoside Rb1 onto QKI was kept for molecular dynamics simulations.

Molecular dynamics simulations

The highest-scoring pose resulting from the docking of Ginsenoside Rb1 with the PHAX (Q9JJT9), HNRPLL (Q921F4), QKI (Q9QYS9) and EIF4G1 (Q6NZJ6) structure underwent refinement through MD simulations. Employing the CHARMM 36 forcefield, interactions between the ligand and protein were computed. MD simulations were carried out within a cubic grid box at a constant temperature of 300 K and pressure of 1 atm. Long-range electrostatic interactions were evaluated using the particle-mesh Ewald method, while temperature control relied on the V-rescale method. Solvation was achieved using TIP3P water molecules. The equilibration process comprised NVT and NPT steps, spanning a duration of 100 ps. The 100-ns MD simulation employed a time step of 2 fs, adopting the Parrinello-Rahman method. Evaluation of complex stability via RMSD guided the selection of the largest cluster for protein–ligand interaction analysis.

Cellular thermal shift assay

After MC38 cells were incubated with Rb1 or control DMSO for 18 h, the cells were collected into PCR tubes (100 μL) and incubated at a series of temperatures from 37 °C to 67 °C, with a gradient of 5 °C for 3 min. After being frozen by using liquid nitrogen and thawed on ice for twice, the supernatant was collected for detecting the PHAX, HNRPLL, QKI and EIF4G1 protein level by western blot.

Surface plasmon resonance

Recombinant PHAX, HNRPLL, QKI and EIF4G1 proteins were coupled onto a CM5 chip (#BR-1005–30) via carboxyl groups on the dextran. After incubation, a series concentration of Rb1 flowed through the protein-CM5 system. The binding was tested and analyzed using Biacore T200 instrument.

Statistical analysis

Statistical analysis was carried out using GraphPad Prism 9 software and SPSS 26.0. All the data were presented as the mean values ± standard deviation (SD). Normality of distribution was determined by Kolmogorov–Smirnov test and variance between groups was assessed by the F-test. For normally distributed data, significance of mean differences was determined by unpaired Student's t-tests. For groups that differed in variance, unpaired t-test with Welch's correction was performed. For data that were not normally distributed, ANOVA was used for different groups analysis. Correlations were determined by Pearson's r coefficient. A two-tailed P value of 0.05 or

less was considered statistically significant. Additional methods and materials are described in the Supplementary Methods.

Results

Circ-0034880-enriched plasma EVs correlate with CRLM

Utilizing the human blood exosome database (exoRBase 2.0), we identified several circRNAs that were significantly more enriched in the plasma EVs of CRC patients compared to those of healthy volunteers (Fig. 1A). Simultaneously, through analysis of the GSE159669 array, multiple circRNAs exhibited markedly higher levels in tumor tissues than in peritumoral tissues (Fig. 1B). Using Venn diagram analysis, we identified 13 highly upregulated circRNAs as potential targets (Fig. 1C).

Next, we initially assessed the expression levels of the aforementioned 13 circRNAs in various human CRC cell lines. Nearly all of these circRNAs demonstrated elevated levels both intracellularly and within EVs of CRC cells compared to normal intestinal epithelial cells (Fig. 1D, Fig. S1). To further validate the clinical significance of these 13 circRNAs, we isolated high-quality EVs from the plasma of CRC patients and healthy volunteers (Fig. 1E, F, G). The qPCR results demonstrated that, among all 13 circRNAs, 10 showed higher expression levels in the plasma EVs of primary CRC patients compared to healthy volunteers, suggesting that these 10 circRNAs may be associated with the progression of CRC. Furthermore, we found that among these 10 circRNAs, only circ-0034880 showed significantly higher expression level in the plasma EVs of CRC patients with liver metastases compared to primary CRC patients, implying that it may be closely related to the occurrence of liver metastasis in CRC (Fig. 1H, I, Fig. S2, Table S2). This clinical data encouraged us to focus on studying the critical relationship between circ-0034880-enriched TEVs and CRLM.

Consistent with the results of clinical blood sample testing, circ-0034880 also exhibited significantly higher expression levels in the EVs of CRC cells compared to human normal intestinal epithelial cells (Fig. 1J). Additionally, our further examination revealed high gene homology between mmu-circ-0034880 and has-circ-0034880 (Fig. S3A), and subsequent validation confirmed elevated expression of mmu-circ-0034880 in the EVs of murine colon cancer cells compared to mouse normal intestinal epithelial cells (Fig. 1K, Fig. S3B).

Above findings prompted us to analyze the expression level of circ-0034880 in primary and liver metastatic tissues of CRC patients. As anticipated, circ-0034880 expression was significantly higher in the liver metastatic tissues compared to primary CRC tissues (Fig. 1L, M), while its expression was minimal in peritumoral tissues (Fig. S4A, B), indicating a close association between circ-0034880-enriched EVs derived from the plasma of CRC patients and CRLM. Furthermore, FISH detection confirmed elevated expression of has-circ-0034880 and mmu-circ-0034880 in multiple colon cancer cells compared to normal intestinal epithelial cells (Fig. 1N and O, Fig. S5).

Circ-0034880-enriched TEVs promote CRLM *in vivo*

To further investigate the *in vivo* effect of circ-0034880-enriched TEVs on CRC liver metastasis, we conducted *in vivo* tracking experiments revealing that

(See figure on next page.)

Fig. 1 Circ-0034880-enriched plasma EVs correlate with CRLM. **A** Human blood exosomes database (exoRBase) was applied to analyze the differentially expressed circRNAs in the plasma EVs of 12 CRC patients and 32 healthy volunteers. Red represents high expression and blue represents low expression. The color brightness of each unit is associated with differences in multiples (log 2[AR/N]). Not all the circRNAs in the figure were labeled. **B** GSE159669 array from GEO database was used to analyze the differentially expressed circRNAs in CRC primary tumor and paired para-carcinoma tissues. Red represents high expression and blue represents low expression. The color brightness of each unit is associated with differences in multiples (log 2[AR/N]). Not all the circRNAs in the figure were labeled. **C** The top up-regulated circRNAs were screened out through the cross-comparative analysis of circRNAs between plasmas and tissues by Venn diagram assay. Red represents upregulated expressed circRNAs in CRC tissues, blue represents upregulated expressed circRNAs in CRC EVs, and pink represents common upregulated expressed circRNAs. **D** Heatmap for 13 upregulated expressed circRNAs in the intracellular space and EVs of human CRC cell lines and colonic epithelial cells NCM460. **E** EVs derived from representative healthy volunteer and CRC patient were analyzed for phenotype (purity and shape) by electron microscopy, and the red arrows indicate the representative separated EVs. Scale bar, 100 nm. **F** EVs derived from representative healthy volunteer and CRC patient were analyzed for size and particle number by LM10 nanoparticle characterization system. **G** Immunoblotting assays of TSG101, CD81 and β-actin in representative EVs derived from healthy volunteer and CRC patients (H: healthy volunteer; P: primary CRC; M: metastatic CRC). **H** qPCR validation and proportion analysis of 13 circRNAs in the EVs derived from healthy volunteer ($n=21$), Primary CRC ($n=60$): plasma from CRC patients without metastases, Metastatic CRC ($n=60$): plasma from CRC patients with liver metastases. **I** qPCR detection data of circ-0034880 in the EVs derived from healthy volunteer ($n=21$), Primary CRC ($n=60$) and Metastatic CRC ($n=60$). **J** qPCR detection data of circ-0034880 in the EVs of human CRC cell lines and colonic epithelial cells NCM460. **K** qPCR detection of circ-0034880 in the EVs of murine colon cancer cell lines MC38 and colonic epithelial cells MODEK. **L**, **M** FISH and quantitative assay of circ-0034880 in the tissues from Primary CRC: primary tissues from CRC patients without metastases, Metastatic CRC: metastatic tissues from CRC patients with liver metastases. Scale bar, 50 μm. **N** FISH detection of has-circ-0034880 in representative human CRC lines LoVo and colonic epithelial cells NCM460. Scale bar, 25 μm. **O** FISH detection of mmu-circ-0034880 in representative murine colon cancer cell lines MC38 and murine colonic epithelial cells MODEK. Scale bar, 25 μm

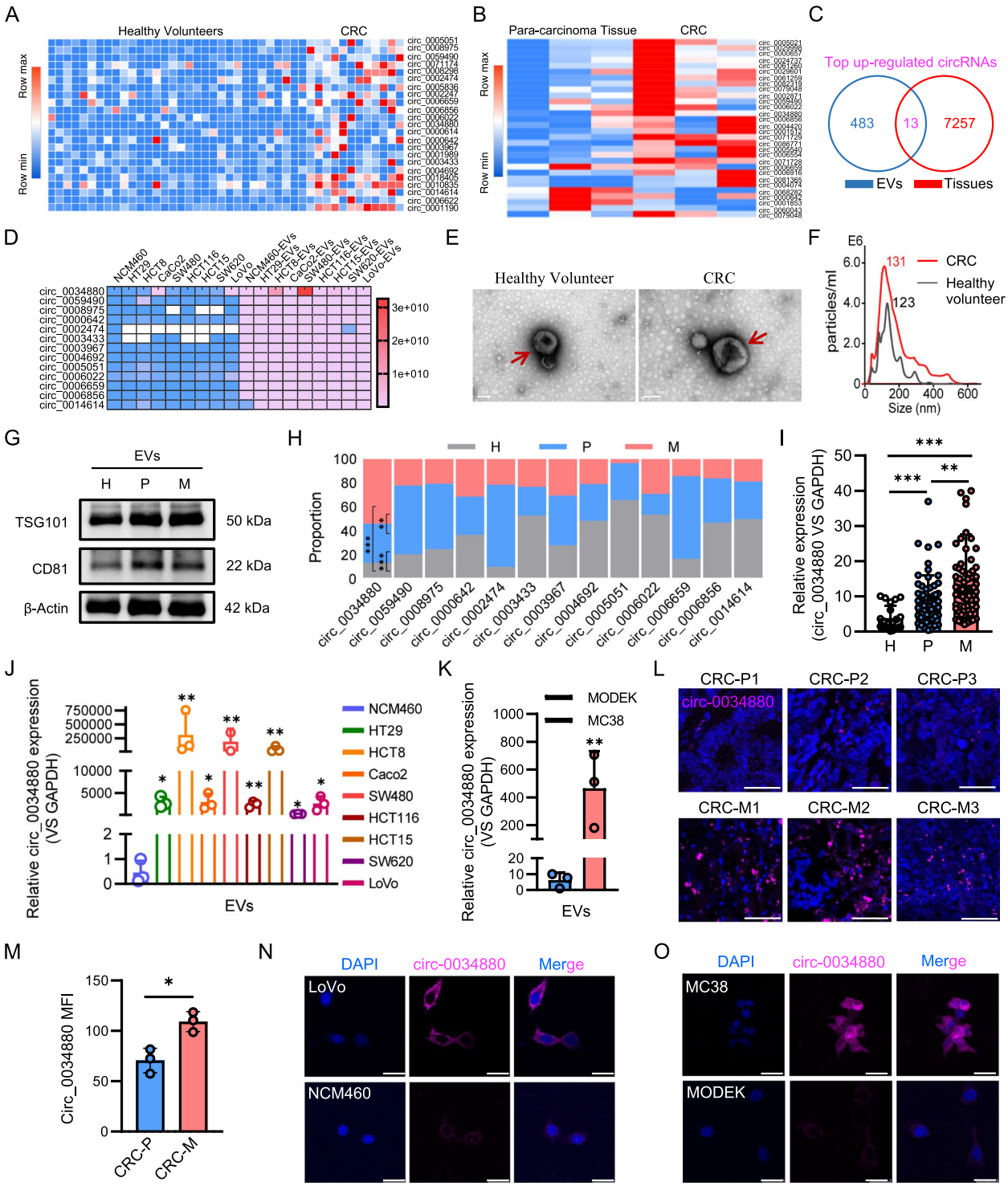

Fig. 1 (See legend on previous page.)

DiR-labeled TEVs accumulated at a high level in liver and lung tissues, with only weak signals observed in spleen, brain, heart and kidney tissues (Fig. 2A, B, Fig. S6A). Subsequently, C57BL/6 J mice were pretreated with TEVs containing varying levels of circ-0034880 (Fig. 2C) for 3 weeks, followed by intrasplenic injection of tumor cells to establish experimental liver metastasis models (Fig. 2D). *In vivo* imaging results demonstrated

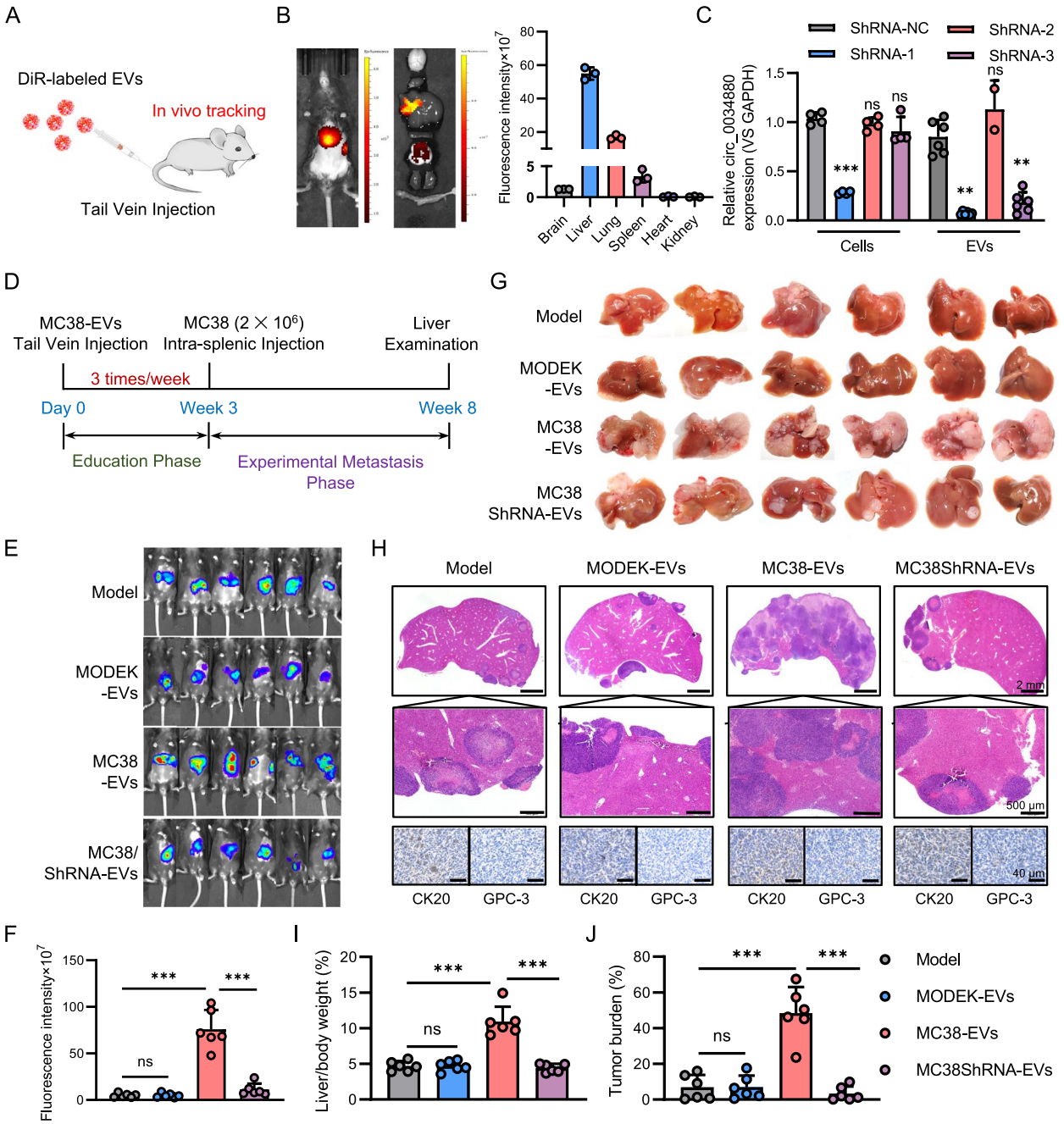

Fig. 2 Circ-0034880-enriched TEVs promote CRC liver metastasis. **A** Flow chart of animal model establishment for TEVs biodistribution observation. **B** Biodistribution of TEVs in the potential metastatic organs of mice. Representative bioluminescent images of mice in indicated groups were shown. **C** qPCR assay of silenced efficiency of circ-0034880 in MC38 cells. **D** Flow chart of animal model establishment for experimental liver metastasis. **E**, **F** Luciferase-based bioluminescence imaging on experimental liver metastasis of the indicated mice treated without EVs or with EVs derived from MODEK cells, or circ-0034880-enriched MC38 cells, or circ-0034880-silenced MC38 cells (shRNA-1 in Fig. 2C was used for K/D of circ-0034880). $n=6$ for each group. Representative bioluminescent images of mice in indicated groups were shown in Fig. 2E, and the quantification data (fluorescence intensity) was presented in Fig. 2F. **G**, **I** Photograph and quantification of liver metastatic tissues $n=6$ for each group. Representative images of liver tissues in indicated groups were shown in Fig. 2G, and the quantification data (liver/body weight, %) was presented in Fig. 2I. **H**, **J** Representative HE staining pictures of liver tissue sections from indicated mice were shown in Fig. 2H (up and middle). In addition, the representative immunohistochemical results using anti-CK20 and anti-glypican-3 (GPC-3) antibody were also shown in Fig. 2H to indicate that the metastatic origin of tumor in liver tissues are from colon tissues (down). The quantification data (tumor burden, %) for HE staining results was presented in Fig. 2J. Scale bar, 2 mm (up), 500 μm (middle), 40 μm (down). All results were shown as mean ± SD. Student's t-test was used to analyze the data. $^{*}P<0.05$; $^{**}P<0.01$

that circ-0034880-enriched TEVs derived from colon cancer cells significantly promote liver metastasis. Conversely, after silencing circ-0034880, the ability of its corresponding TEVs to promote liver metastasis markedly decreased (Fig. 2E, F). After 8 weeks of the experiment, all mice were euthanized. The tumor foci (Fig. 2G, Fig. S7) and liver/body weight ratio (Fig. 2I) were all obviously increased in circ-0034880-enriched TEVs group compared with the model group and negative control group. However, after silencing circ-0034880, the ability of its corresponding TEVs to increase the tumor foci and liver/body weight ratio significantly reduced (Fig. 2G, I). In agreement with the above observation, H&E staining also showed significant increase of tumor burden in circ-0034880-enriched TEVs group compared with the model group and negative control group, but obvious elimination of tumor burden in circ-0034880-silencing TEVs group compared with the circ-0034880-enriched TEVs group (Fig. 2H, J). It is noteworthy that the baseline expression of circ-0034880 in normal mouse liver tissue was extremely low (Fig. S6B).

Circ-0034880-enriched TEVs activate CD206$^+$ pro-tumor macrophages in liver pre-metastatic microenvironment

To comprehensively assess the impact of circ-0034880-enriched TEVs on the pre-metastatic microenvironment in the liver, we established a specialized mouse model for TEVs education and experimental liver metastasis (Fig. 3A). Mice were educated with EVs or TEVs containing different levels of circ-0034880 via tail vein injection every other day for 3 weeks. After one week of EVs or TEVs education, experimental liver metastasis model was prepared by intra-splenic injection of murine tumor cells in mice. Another two weeks later, the mice liver metastatic lesions were obtained to investigate the effects of TEVs on the whole liver pre-metastatic microenvironment. The multiplexed immunofluorescence analysis revealed that circ-0034880-enriched TEVs induced significant infiltration of CD11B$^+$ macrophages and α-SMA$^+$ fibroblasts, particularly CD11B$^+$CD206$^+$ pro-tumor macrophages (Fig. 3B). This suggests that circ-0034880-enriched TEVs may primarily influence liver macrophages, reshaping the liver microenvironment. Previous studies have consistently shown the tumor-promoting effects of pro-tumor macrophages [14, 25, 26]. Our flow cytometry results further validated the stimulatory effect of circ-0034880-enriched TEVs on CD11B$^+$ macrophages infiltration, particularly CD11B$^+$CD206$^+$ pro-tumor macrophages, within the liver microenvironment (Fig. 3C, D). Furthermore, using the mice liver metastases data from Fig. 2E, we confirmed a positive correlation between circ-0034880 expression levels and CD206$^+$ pro-tumor TAM infiltration (Fig. 3E, F, Fig. S8). Additionally, compared to primary CRC tissues, higher circ-0034880 expression was detected in CRC liver metastatic lesions, showing a positive correlation with CD206$^+$ pro-tumor TAMs infiltration (Fig. 3G, H, I).

Circ-0034880-enriched TEVs promote CRC cells migration via activating CD206$^+$ pro-tumor macrophages

Since several reports have shown the promoting effect of activated macrophages on CRC cell migration [27–29], we further investigated the effects of circ-0034880-enriched TEVs on CRC cells migration and CD206$^+$ pro-tumor macrophages *in vitro*. To track the delivery of EVs to macrophages, EVs derived from murine colon cancer cells and normal murine BMDMs were labeled with DiR (red) and DiO (green), respectively. Confocal imaging revealed the presence of red spots in recipient BMDMs after co-incubation, indicating successful delivery of EVs to macrophages (Fig. 4A). Subsequently, we observed a significant increase in circ-0034880 levels in macrophages following co-culture with TEVs derived from murine colon cancer cells. However, there was minimal change in the co-culture group with TEVs derived from circ-0034880-silenced murine colon cancer cells compared to the EVs derived from murine intestinal epithelial cells with extremely low endogenous expression of

(See figure on next page.)

Fig. 3 Circ-0034880-enriched TEVs activate CD206$^+$ pro-tumor macrophages in liver pre-metastatic microenvironment. **A** Flow chart of mice model establishment for detecting the effect of TEVs on the liver pre-metastatic microenvironment. **B** Multiplexed immunofluorescence assay was used to detect the overall effect of TEVs on the phenotype in the pre-metastatic microenvironment (left: 7 days; right: 14 days). The resected liver tissues were stained with antibodies against CD11B, CD206, α-SMA, Ly6G and CD3. Nuclear staining was done with DAPI. Scale bar, 20 μm (D7), 25 μm (D14). **C**, **D** Effect of TEVs on macrophages in the liver pre-metastatic microenvironment was detected by flow cytometry (7 days and 14 days). **E** FISH and quantitative assay of circ-0034880 in the liver metastatic tissues from Fig. 2E. Scale bar, 50 μm. **F** Immunofluorescence analysis of TAMs in the liver metastatic tissues from Fig. 2E. The 6 μm O.C.T. tissue cryosections were stained with antibodies against F4/80 and CD206. Nuclear staining was done with DAPI. Scale bar, 50 μm. **G**, **H** FISH and immunofluorescence assay of circ-0034880 expression in TAMs form representative clinical primary CRC and CRC liver metastatic lesions. Antibodies against CD86 and CD206 were stained for TAMs, and FITC labelled circ-0034880 probe was applied for circ-0034880 detection. **I** Correlation between circ-0034880 expression and CD206 expression in above TAMs form representative clinical primary CRC and CRC liver metastatic lesions. Scale bar, 20 μm. All results were shown as mean ± SD. Student's t-test was used to analyze the data. *, $P < 0.05$; **, $P < 0.01$

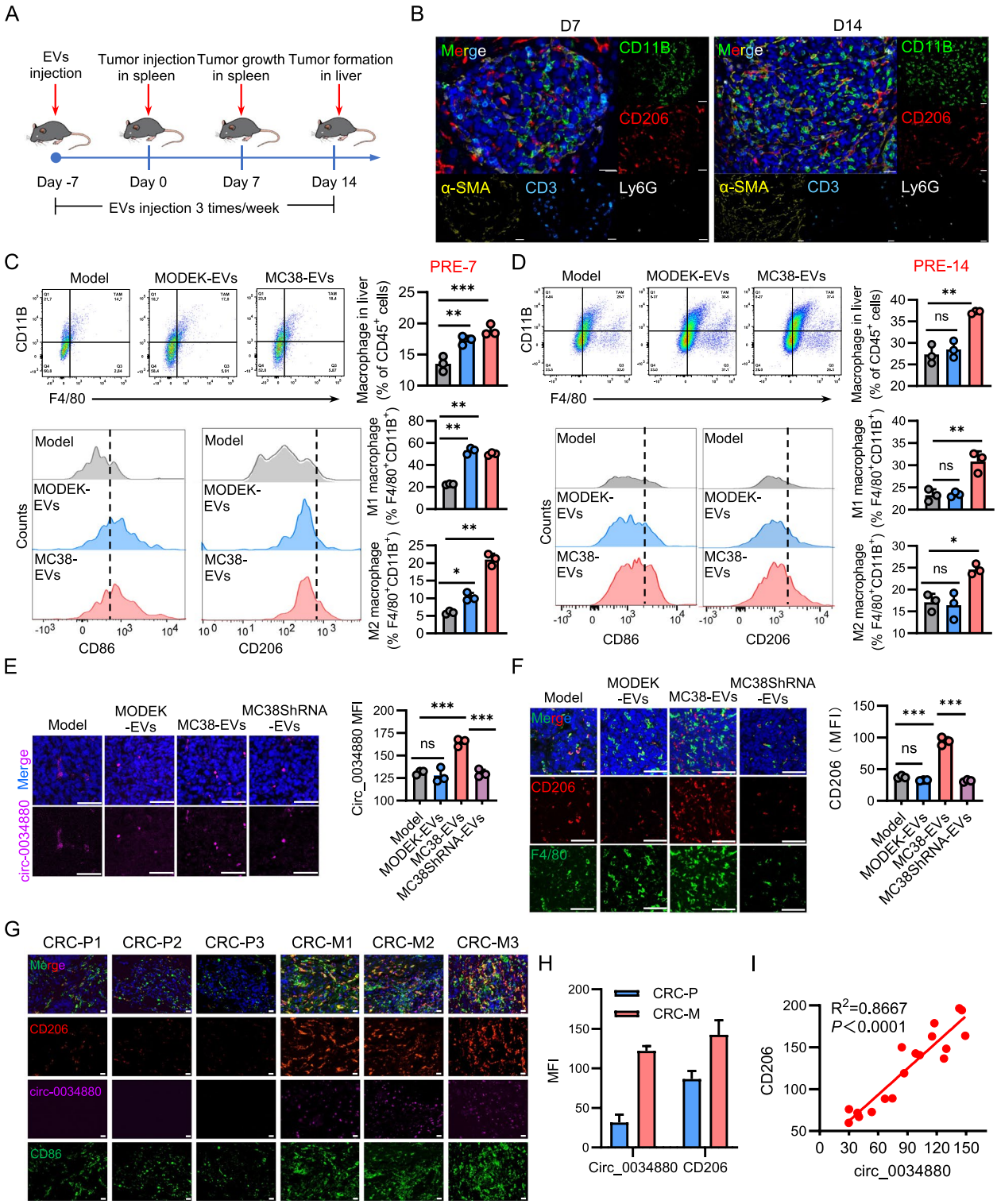

Fig. 3 (See legend on previous page.)

circ-0034880 (Fig. 4B, C). This suggests that circ-0034880 was transferred to macrophages from cancer cells in the form of TEVs.

Furthermore, functional experiments demonstrated that circ-0034880-enriched TEVs could promote the activation of $CD206^+$ pro-tumor macrophages (Fig. 4D, E,

F). Additionally, conditioned medium corresponding to circ-0034880-enriched TEVs significantly promote the migration of colon cancer cells (Fig. 4G, H). These *in vitro* experiments collectively suggest that circ-0034880-enriched TEVs promote CRC cells migration by activating $CD206^+$ pro-tumor macrophages.

Circ-0034880-enriched TEVs facilitate the activation of $SPP1^{high}CD206^+$ pro-tumor macrophages

Although previous *in vitro* and *in vivo* experiments suggest that circ-0034880 influences the activation of $CD206^+$ pro-tumor macrophages, the specific regulatory mechanism remains unclear. To elucidate this mechanism, we first analyzed the transcriptome data of BMDMs pretreated with or without TEVs derived from murine colon cancer cells. The volcanic plot in Fig. 5A illustrates that 732 genes were upregulated in BMDMs pretreated with TEVs compared to control BMDMs. Similarly, Fig. 5B shows that 555 genes were downregulated in BMDMs pretreated with circ-0034880-silenced TEVs compared to the TEVs group. Subsequent Venn diagram analysis revealed 95 common alerted genes (Fig. 5C), with the heatmap in Fig. 5D displaying the top 30 differentially expressed genes.

Among these genes, SPP1 and Phlda1 were the downregulated genes with statistical significance after circ-0034880 silencing (Fig. 5E). Because our previous experiments have confirmed a close correlation between the expression of circ-0034880 and the activation of pro-tumor macrophages (Fig. 4D, E, F), we further supplement the experiment to explore whether the knockdown of SPP1 or Phlda1 gene is also positively correlated with the activation of pro-tumor macrophages. The qPCR results confirmed that under the knockdown of the SPP1 gene, the activation effect of IL-4 or TEVs on pro-tumor macrophages was significantly reduced (Fig. S9A). However, under the knockdown of the Phlda1 gene, the activation effect of IL-4 or TEVs on pro-tumor macrophages was affected minimally (Fig. S9B). Moreover, the literature search results also indicate that SPP1 is known to be abundantly expressed in tumor metastatic tissues [30, 31], with $SPP1^+$ macrophages being predominant in CRLM [32]. Therefore, above preliminary experimental and literature search results jointly suggest that the SPP1 gene may be a key bridge for circ-0034880 to affect the activation of pro-tumor macrophages, but the function and regulatory mechanism by which the Phlda1 gene participates in needs further research in the future.

Subsequently, multiple *in vitro* experiments demonstrated a positive correlation between the mRNA and protein expression levels of SPP1 and the expression of circ-0034880, as well as the activation of $CD206^+$ pro-tumor macrophages (Fig. 5F, G, H, I). To validate the *in vitro* findings, we examined SPP1 expression in experimental mouse liver metastatic and clinical liver metastatic tissues. Notably, SPP1 is a secretory protein [33], primarily produced by macrophages [34]. Immunofluorescence experiments revealed that SPP1 was mainly secreted into the interstitial tissue of the TME (Fig. 5J). Therefore, in subsequent tissue sample analyses, we focused on observing the overall protein expression of SPP1 in the TME. The immunofluorescence results indicated significantly higher SPP1 protein expression in TEVs-pretreated experimental mouse liver metastatic tissues, but significantly lower expression in the circ-0034880-silenced TEVs-pretreated group (Fig. S10A). Importantly, clinical samples also confirmed the significantly upregulated SPP1 protein expression in the TME of CRC liver metastatic tissues (Fig. S10B). Taken together, these findings suggest that circ-0034880-enriched TEVs facilitate the activation of $SPP1^{high}CD206^+$ pro-tumor macrophages.

TEVs-released circ-0034880 elevates SPP1 expression in macrophages by protecting SPP1 from miR-200a-3p and miR-141-3p-mediated degradation

Given that circRNAs are known to function as miRNAs sponges, we aimed to identify the potential miRNAs linking circ-0034880 and SPP1. Utilizing the Circular RNA Interactome database and RegRNA, we identified miR-200a-3p and miR-141-3p as putative targets of circ-0034880 (Fig. 5K, L). Since AGO2 protein plays a crucial role in circRNAs or miRNAs regulating gene expression, we initially investigated the interaction

(See figure on next page.)

Fig. 4 Circ-0034880-enriched TEVs promote CRC cells migration via activating $CD206^+$ pro-tumor macrophages. **A** Confocal imaging showed the delivery of DiR-labeled EVs (red) to DiO-labeled BMDMs (green). Scale bar, 25 μm. **B** FISH detection of circ-0034880 in representative BMDMs treated with MC38-EVs or MC38shRNA-EVs for 48 h. Scale bar, 25 μm. **C** qPCR detection of circ-0034880 in representative BMDMs treated with MC38-EVs or MC38shRNA-EVs for 24 h and 48 h. **D** Immunofluorescence analysis of $CD206^+$ macrophages in BMDMs treated with MC38-EVs or MC38shRNA-EVs. The BMDMs were stained with antibodies against F4/80 and CD206. Nuclear staining was done with DAPI. Scale bar, 25 μm. **E**, **F** qPCR detection of macrophages activation associated genes (Arg-1, CD206, VEGF, CD274, iNOS, H2-Ab1) in BMDMs treated with MC38-EVs or MC38shRNA-EVs for 48 h. **G**, **H** Transwell and wound healing assay of MC38 cells treated with indicated conditioned medium (CM) from BMDMs that pretreated with IL-4, MC38-EVs, or MC38shRNA EVs, or none. Representative images were shown and migrated cells were counted. Scale bar, 150 μm. Scale bar, 150 μm. All results were shown as mean ± SD. Student's t-test was used to analyze the data. *, $P < 0.05$; **, $P < 0.01$

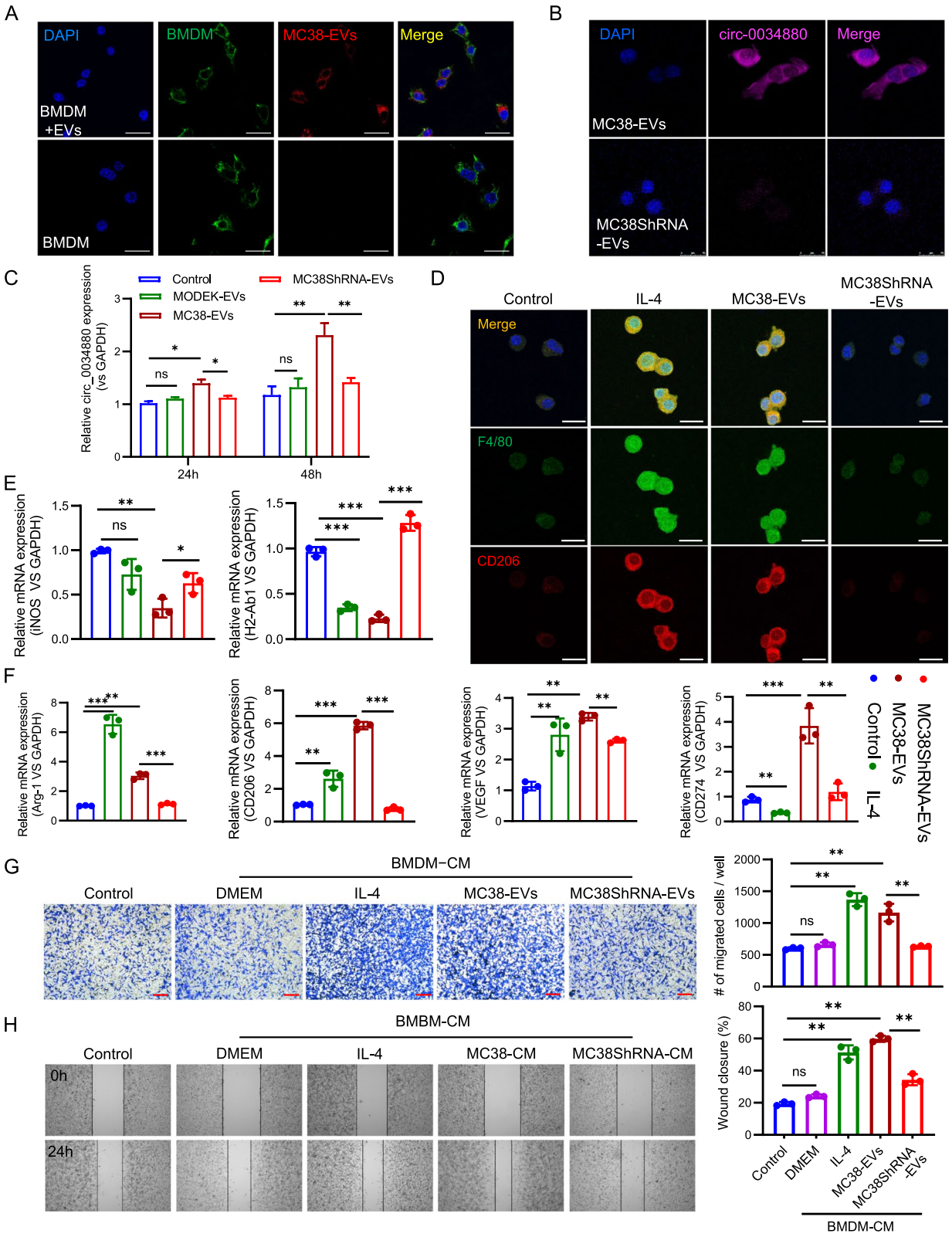

Fig. 4 (See legend on previous page.)

between circ-0034880 and AGO2 or between miRNAs and AGO2. RIP assays revealed an enrichment of circ-0034880 in anti-AGO2 immunoprecipitates (Fig. 5M), along with the enrichment of miR-200a-3p and miR-141-3p (Fig. 5N). To further confirm these results, we repeated the interaction experiments in macrophages by using the murine BMDMs. The supplementary experiments confirmed the interaction between circ-0034880 and AGO2 or between miR-200a-3p/miR-141-3p and AGO2 in macrophages (Fig. S11).

To confirm the interaction between circ-0034880 and miR-200a-3p or miR-141-3p, we synthesized wild-type or mutant circ-0034880 fragments containing the predicted binding site of the identified miRNAs and inserted them downstream of the dual-luciferase reporter gene (Fig. S12A). Luciferase assay results indicated that both miR-200a-3p and miR-141-3p mimics decreased the relative luciferase activity, while the luciferase activity of the circ-0034880 mutant group remained unchanged (Fig. 5O).

Similarly, to validate the interaction between miR-200a-3p/miR-141-3p and SPP1, we synthesized wild-type or mutant SPP1 mRNA 3'UTR fragments containing the predicted binding site of the identified miRNAs and inserted them downstream of the dual-luciferase reporter gene (Fig. S12B). The dual-luciferase assay demonstrated that both miR-200a-3p and miR-141-3p mimics significantly decreased the luciferase reporter activity of the wild-type SPP1-3'UTR, whereas the luciferase activity of the mutant SPP1-3'UTR remained unaltered (Fig. 5P). In summary, our findings collectively demonstrate that TEVs-released circ-0034880 elevates SPP1 expression in macrophages by protecting SPP1 from miR-200a-3p and miR-141-3p-mediated degradation.

Ginsenoside Rb1 administration prevents CRC cells migration by impeding circ-0034880-enriched TEVs mediated activation of SPP1^{high}CD206^{+} pro-tumor macrophages

To identify potential therapeutic drugs targeting specific molecules such as circ-0034880, we conducted a screening of 103 natural products. Following preliminary dose screening, 71 natural products were selected to investigate their effects on circ-0034880 expression (Table S3). Through qPCR analysis, four natural products including Ginsenoside Rb1, Isorhamnetin, Kaempferol, and Quercetin exhibited the most potent inhibitory effects on circ-0034880 expression (Fig. 6A, Fig. S13A). Among these, Ginsenoside Rb1 emerged as the ideal candidate drug for subsequent anti-tumor metastasis studies (Fig. 6C, Fig. S13B, C) due to its better inhibitory function on TEVs secretion (Fig. 6B).

Further analysis revealed that Ginsenoside Rb1 effectively inhibited circ-0034880 expression, similar to direct circ-0034880 silencing, as evidenced by FISH results (Fig. 6D, E). However, under the premise of circ-0034880 silencing, the circ-0034880 expression remained unaltered after plus treatment with Ginsenoside Rb1 (Fig. 6D, E). Additionally, qPCR assays of circ-0034880 in colon cancer cell-derived TEVs confirmed these findings (Fig. 6F).

Given the inhibitory effect of Ginsenoside Rb1 on circ-0034880 expression, we investigated whether Ginsenoside Rb1 could affect the activation of SPP1^{high}CD206^{+} pro-tumor macrophages via circ-0034880-enriched TEVs.

(See figure on next page.)

Fig. 5 Circ-0034880-enriched TEVs facilitate the activation of SPP1^{high}CD206^{+} pro-tumor macrophages by protecting SPP1 from miR-200a-3p and miR-141-3p-mediated degradation. **A**, **B** Volcano plots of log2 fold change (FC) and log10 adjusted *p* value of differentially expressed genes between MC38-EVs-treated BMDMs and control BMDMs or between MC38-EVs-treated BMDMs and MC38shRNA-EVs-treated BMDMs. MC38shRNA-EVs represents EVs derived from MC38 cells of circ-0034880 silencing. **C** Venn diagram assay of up-regulated genes in MC38-EVs-treated BMDMs and down-regulated genes in MC38shRNA-EVs-treated BMDMs. **D** Heatmap of top 30 upregulated and downregulated genes. **E** qPCR validation of the top 10 differentially expressed genes in BMDMs treated with or without circ-0034880 gene silencing. **F** qPCR detection of SPP1 gene in BMDMs that pretreated with IL-4, MC38-EVs, or MC38shRNA EVs, or none. **G** Immunoblotting and quantitative assays of SPP1 in BMDMs that pretreated with IL-4, MC38-EVs, or MC38shRNA EVs, or none. **H** Immunofluorescence and quantitative analysis of SPP1 in BMDMs that pretreated with IL-4, MC38-EVs, or MC38shRNA EVs, or none. Scale bar, 25 μm. **I** ELISA and quantitative assays of SPP1 levels in the supernatant of BMDMs that pretreated with IL-4, MC38-EVs, or MC38shRNA EVs, or none. **J** Immunofluorescence analysis of SPP1 and CD206 in the mice liver metastatic tissues from Fig. 2E. Antibody against SPP1 and CD206 were used in this part. Yellow arrow represents SPP1 in TAMs (CD206^{+}), white arrow represents SPP1 in the whole mesenchyme of TME. Scale bar, 20 μm. **K** CircRNA interactome databases and RegRNA were used to predict the potential target miRNAs of circ-0034880 and SPP1, respectively. Venn diagram showed the mutual putative target miRNAs of circ-0034880 and SPP1. **L** MiR-200a-3p and miR-141-3p were selected as the potential bridge between circ-0034880 and SPP1. **M** Interaction between circ-0034880 and AGO2 protein was confirmed by RIP and qPCR assay in H293T cells. **N** Potential miRNAs (miR-200a-3p and miR-141-3p) that bind with circ-0034880 were detected by qPCR using the anti-AGO2 immunoprecipitates. **O** Luciferase reporter activity was measured in H293T cells after co-transfection with circ-0034880-WT or circ-0034880-MUT and miR-200a-3p/miR-141-3p mimics. **P** Luciferase reporter activity was measured in H293T cells after co-transfection with SPP1 3'UTR-WT or SPP1 3'UTR-MUT and miR-200a-3p/miR-141-3p mimics. All results were shown as mean ± SD. Student's t-test was used to analyze the data. *, $P < 0.05$; **, $P < 0.01$

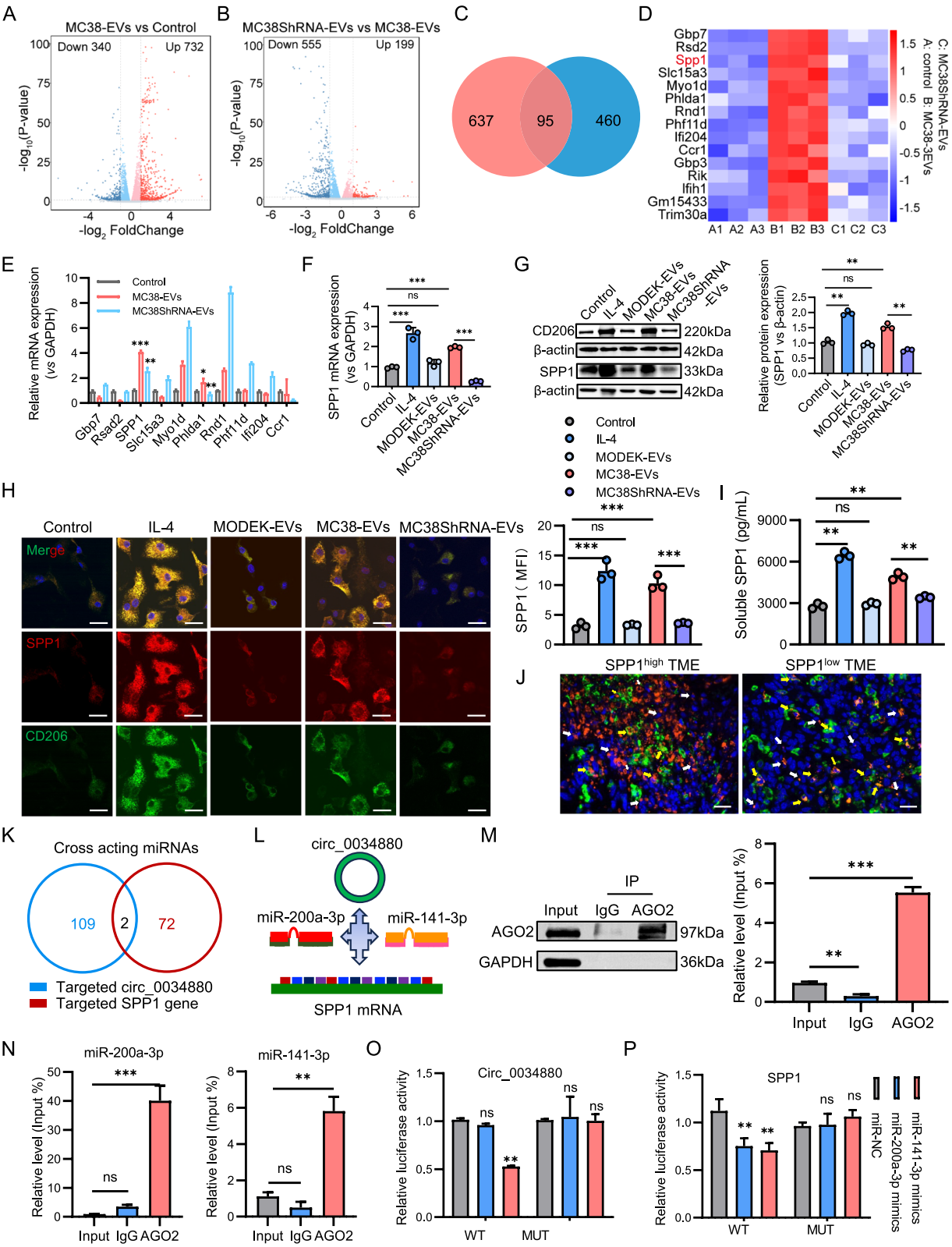

Fig. 5 (See legend on previous page.)

Consistent with the expression levels in corresponding colon cancer cells, levels of circ-0034880 in BMDMs treated with different TEVs mirrored those findings, with Ginsenoside Rb1 administration notably reducing circ-0034880 levels in BMDMs (Fig. 6G, H, I). Furthermore, protein expression of SPP1 in BMDMs was significantly downregulated following Ginsenoside Rb1 treatment, akin to direct circ-0034880 silencing (Fig. 6J, K). Nevertheless, under the premise of silencing circ-0034880, the protein expression of SPP1 in BMDMs affected by Rb1 was slightly altered (Fig. 6J, K). ELISA and qPCR experiments further supported these results (Fig. 6L, M).

Moreover, as shown in Fig. 6N, Fig. S14, circ-0034880-enriched TEVs elevated the mRNA expression levels of the markers of pro-tumor macrophages, whereas the mRNA expression levels of the markers of pro-inflammatory macrophages were decreased. Nevertheless, both circ-0034880 silencing and Ginsenoside Rb1 administration reversed the effect of circ-0034880-enriched TEVs on the markers of pro-tumor and pro-inflammatory macrophages. Additionally, under the premise of circ-0034880 silencing, Ginsenoside Rb1 administration had little effect on the markers of pro-tumor and pro-inflammatory macrophages, suggesting that Rb1 impedes circ-0034880-enriched TEVs mediated activation of $CD206^+$ pro-tumor macrophages (Fig. 6N, Fig. S14). Importantly, in human colon cancer cell lines, we also confirmed the inhibitory effect of Ginsenoside Rb1 on the activation of $CD206^+$ pro-tumor macrophages (Fig. S15A).

Furthermore, conditioned media from indicated BMDMs significantly reduced the migratory ability of colon cancer cells, similar to the effect of the direct circ-0034880 silencing. However, under the premise of silencing circ-0034880, the migratory ability remained largely unchanged following Ginsenoside Rb1 administration (Fig. 6O, P). Similar inhibitory effect of Ginsenoside Rb1 on the migration of human colon cancer cell lines were also observed (Fig. S15B). In conclusion, our results demonstrate that Ginsenoside Rb1 administration prevents CRC cells migration by impeding circ-0034880-enriched TEVs mediated activation of $SPP1^{high}CD206^+$ pro-tumor macrophages.

Rb1 directly binds to QKI protein to inhibit the biogenesis of circ-0034880

To identify the direct targets of Rb1 that influence circ-0034880 expression, we initially conducted a DARTS assay to screen potential targets of Rb1. The volcanic plot and heatmap in Fig. 7A, B revealed 151 differentially expressed proteins in Rb1-pretreated murine colon cancer cells compared to control cells (see Supplemental Data). As circRNAs biogenesis is tightly regulated by specific proteins, we focused on proteins known or suspected to regulate circRNAs biogenesis through literature mining (Table S4). Venn diagram analysis identified QKI protein as a promising target (Fig. 7C). While proteins like PHAX, HNRPLL and EIF4G1 are essential for mRNA regulation, they were also selected for validation.

Next, we predicted potential ligand binding sites of PHAX, HNRPLL, QKI and EIF4G1 using CavityPlus 2022. As shown in Table S5 and Fig. S16, all of the four proteins possessed cavities with strong druggability, with each protein having one contiguous druggable pocket. Molecular docking simulation assessed the binding potential of Ginsenoside Rb1 to these proteins. The docking score of Rb1 to PHAX, HNRPLL and EIF4G1 was estimated to be -6.689 kcal/mol, -7.829 kcal/mol and -7.674 kcal/mol. This molecule associated with the binding site of PHAX, HNRPLL and EIF4G1 mainly though hydrogen bonds, Pi-alkyl and alkyl interactions (Fig. S17). For instance, the disaccharide groups of Rb1 formed the majority of hydrogen bonds with the protein, and alkyl and Pi-alkyl interactions were formed by the methyl, isobutene and steroid of Rb1 (Fig. S18). Notably, Rb1 was first docked to the druggable pocket of QKI with

(See figure on next page.)

Fig. 6 Rb1 administration prevents CRC cells migration by impeding circ-0034880-enriched TEVs mediated activation of $SPP1^{high}CD206^+$ pro-tumor macrophages. **A** Effects of 71 natural products on the expression of circ-0034880 were measured by qPCR. The Heatmap showed the inhibitory degree of different natural products on circ-0034880 expression. **B** Effects of the selected 4 natural products on the TEVs secretion of MC38 were analyzed by NanoSight. **C** 3D molecular structure diagram of natural product Ginsenoside Rb1. **D**, **E** FISH and quantitative assay of the effects of gene silencing and Ginsenoside Rb1 administration on the expression of circ-0034880 in MC38 cells. Scale bar, 25 μm. **F** qPCR assay of the circ-0034880 expression in the EVs derived from MC38 cells pretreated with gene silencing and/or Ginsenoside Rb1 administration. **G**, **H** FISH and quantitative assay of the effects of different EVs pretreatment on the expression of circ-0034880 in BMDMs. Scale bar, 25 μm. **I** qPCR assay of the effects of different EVs pretreatment on the expression of circ-0034880 in BMDMs. **J**, **K** Immunofluorescence and quantitative analysis of CD206 and SPP1 in the BMDMs treated with DMEM, or MC38-EVs, or MC38shRNA-EVs, or Rb1 + MC38shRNA-EVs. Scale bar, 25 μm. **L** ELISA assays of secretory SPP1 protein in the supernatant of BMDMs treated with DMEM, or MC38-EVs, or MC38shRNA-EVs, or Rb1 + MC38shRNA-EVs. **M** qPCR assay of SPP1 in the BMDMs treated with DMEM, or MC38-EVs, or MC38shRNA-EVs, or Rb1 + MC38shRNA-EVs. **N** qPCR detection of macrophages activation associated genes (Arg-1, CD206, iNOS) in the BMDMs treated with DMEM, or MC38-EVs, or MC38shRNA-EVs, or Rb1 + MC38shRNA-EVs. **O**, **P** Transwell and wound healing assay of the effects of different EVs pretreated BMDMs culture supernatant on CRC cell migration. Scale bar, 150 μm. All results were shown as mean ± SD. Student's t-test was used to analyze the data. *, $P < 0.05$; **, $P < 0.01$

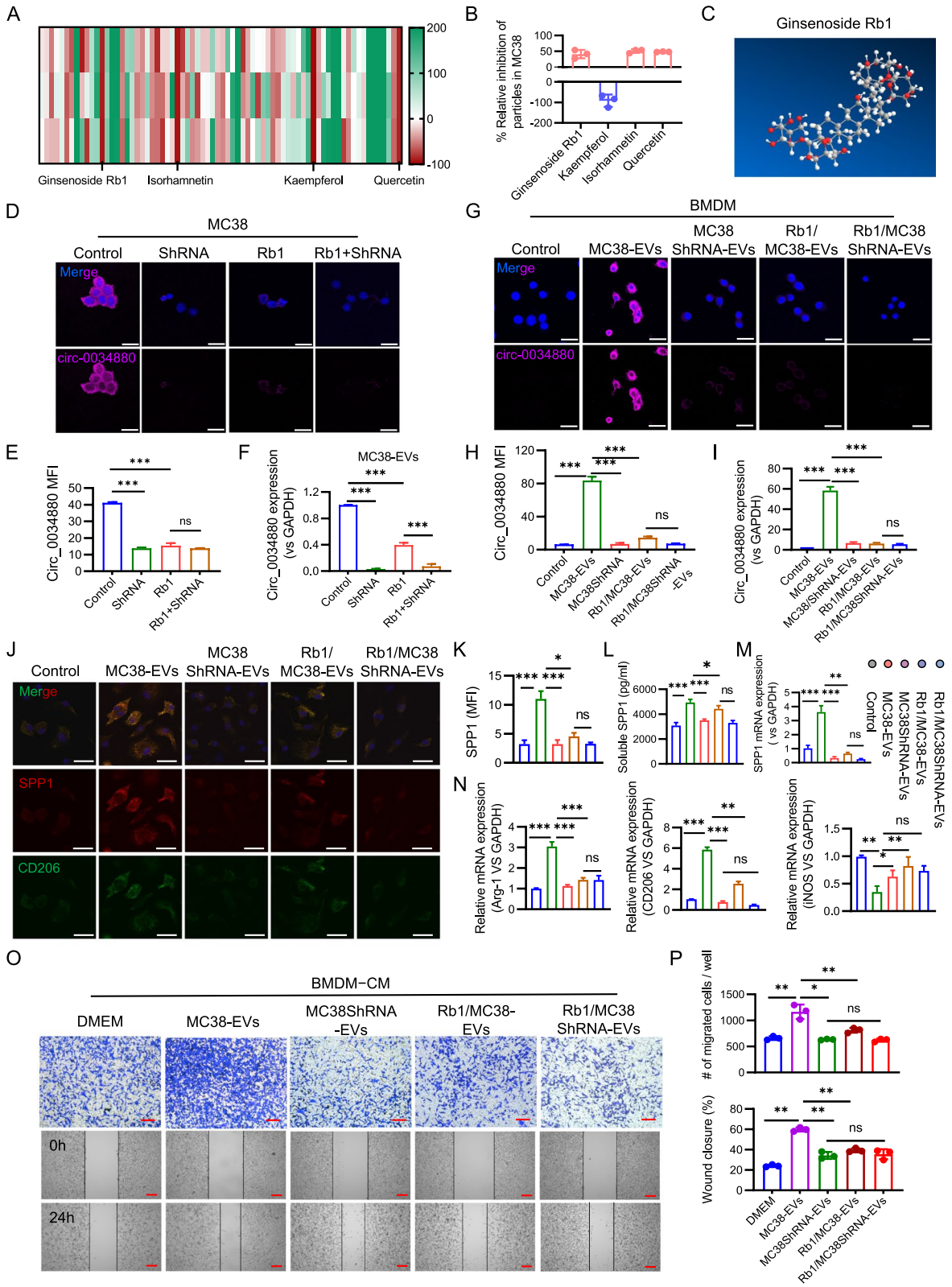

Fig. 6 (See legend on previous page.)

the docking score -5.750 kcal/mol, and firmly bound to QKI during the 100-ns molecular dynamics simulations (RMSD) (Fig. 7D, E). However, the RMSD assay data demonstrated that, HNRPLL (red) and EIF4G1 (green) showed unstable binding with Rb1, PHAX (blue) showed relative stable binding with Rb1 (Fig. S19). Similarly, despite the higher number of hydrogen bonds in the Rb1-QKI complex, the Ginsenoside Rb1 interacted robustly with protein via multiple alkyl interactions (Fig. 7D). These results showed that Rb1 potentially bound to PHAX, HNRPLL and EIF4G1, and formed stable complex with QKI.

QKI protein has been implicated in regulating pre-mRNA splicing and promoting circRNA biogenesis [35, 36]. To validate the computational docking and molecular dynamics simulations results, we performed a CETSA assay, confirming that Rb1 significantly increased the thermal stability of QKI (Fig. 7F, G). However, the effects of Rb1 on the thermal stability of PHAX, HNRPLL and EIF4G1 were not that remarkable (Fig. S20). These results were further supported by an SPR assay, indicating strong affinity between Rb1 and QKI with KD values 1.033e-05 M (Fig. 7H), in compared with the SPR assay results between Rb1 and PHAX (KD values 1.580e-05 M), Rb1 and HNRPLL (KD values 2.168e-03 M), Rb1 and EIF4G1 (unable to fit) (Fig. S21). The high-affinity binding characteristics suggest that QKI might be a biological target of Rb1. Moreover, in Fig. 7I, the computational docking model revealed Rb1 binding to the domain of QKI protein overlapping with its RNA binding domain [37]. The overlapping binding domain suggested a potential competitive relationship between Rb1 and circ-0034880, prompting investigation into the effect of QKI gene silencing on circ-0034880 biogenesis. Indeed, QKI knockdown remarkably suppressed circ-0034880 expression (Fig. 7J, K, L, M), underscoring the role of in mediating the impact of Rb1 on circ-0034880 biogenesis. Taken together, our findings demonstrate that Rb1 directly binds to QKI protein, inhibiting the biogenesis of circ-0034880.

Rb1 administration inhibits CRLM via impeding circ-0034880-enriched TEVs mediated activation of SPP1^{high}CD206^{+} pro-tumor TAMs

To validate the *in vivo* effect of Rb1 administration, we designed a study as depicted in Fig. 8A, outlining Rb1 intervention in a mouse model of experimental liver metastasis. *In vivo* imaging results in Fig. 8B, C demonstrated a significant reduction in the liver metastases in the Rb1-pretreated TEVs administration group compared to the TEVs alone, closely resembling the effect of direct circ-0034880 silencing. However, in the context of circ-0034880 silencing, liver metastases were minimally affected by Rb1-pretreated TEVs administration (Fig. 8B, C). After 5 weeks of the experiment, all mice were euthanized. The tumor foci (Fig. 8D, Fig. S22) and liver/body weight ratio (Fig. 8F) were all obviously decreased in the Rb1-pretreated TEVs administration group compared to the TEVs alone, closely resembling the effect of direct circ-0034880 silencing. However, in the context of circ-0034880 silencing, tumor foci and liver/body weight ratio were minimally affected by Rb1-pretreated TEVs administration (Fig. 8D, F). In agreement with the above observation, H&E staining also showed significant decrease of tumor burden in the Rb1-pretreated TEVs administration group compared to the TEVs alone, closely resembling the effect of direct circ-0034880 silencing (Fig. 8E, G). Nevertheless, in the context of circ-0034880 silencing, the tumor burden was minimally affected by Rb1-pretreated TEVs administration (Fig. 8E, G).

Next, we explored the effects of Rb1 on the infiltration of CD206^{+} pro-tumor TAMs in the liver metastases. Compared to the untreated group, the Rb1-pretreated TEVs administration group exhibited a significant decrease in CD206^{+} pro-tumor TAMs, similar to the effect of the direct circ-0034880 silencing. However,

(See figure on next page.)

Fig. 7 Rb1 directly binds to QKI and inhibits the biogenesis of circ-0034880. **A** DARTS experiment was performed to search the direct targets of Rb1 in MC38 cells. Volcano plots of log2 fold change (FC) and log10 adjusted p value of differentially proteins between Rb1-treated MC38 cells and control MC38 cells. Red dots, proteins upregulated in Rb1-treated MC38 cells; blue dots, proteins upregulated in control MC38 cells. **B** Heatmap of upregulated and downregulated proteins by DARTS assay of Rb1-treated MC38 cells and control MC38 cells. **C** Venn diagram assay of Rb1 targeted proteins ($n = 151$) and circRNAs biogenesis associated proteins ($n = 17$). **D** The stereo view of MD-optimized complex structure of QKI (Q9QYS9, residue14-203) bound with Ginsenoside Rb1 and the detailed interactions between QKI and Ginsenoside Rb1. **E** The RMSD analysis of Ginsenoside Rb1 fitted to the backbone of QKI. **F**, **G** CETSA experiment was used to evaluate the binding between Rb1 and QKI in thermodynamic levels. The expression level of QKI protein was detected by western blot. **H** SPR was performed using QKI full length proteins with increasing concentrations of Rb1. The equilibrium dissociation constant (KD) was evaluated according to the response-concentration curve. **I** The computational docking model showed the Rb1 drug binding domain in QKI protein, and QKI protein shared the same RNA binding domain with Rb1 drug binding domain. The motif of QKI was obtained from ENCORI, and multiple QKI binding sequences were found in the flanking of circ-0034880. **J**, **K**, **L** Expression of QKI mRNA and protein in QKI-silenced MC38 cells and control MC38 cells was measured by qPCR and western blot analysis. **M** Expression of circ-0034880 in QKI-silenced MC38 cells and control MC38 cells were evaluated by qPCR analysis. All results were shown as mean ± SD. Student's t-test was used to analyze the data. *, $P < 0.05$; **, $P < 0.01$

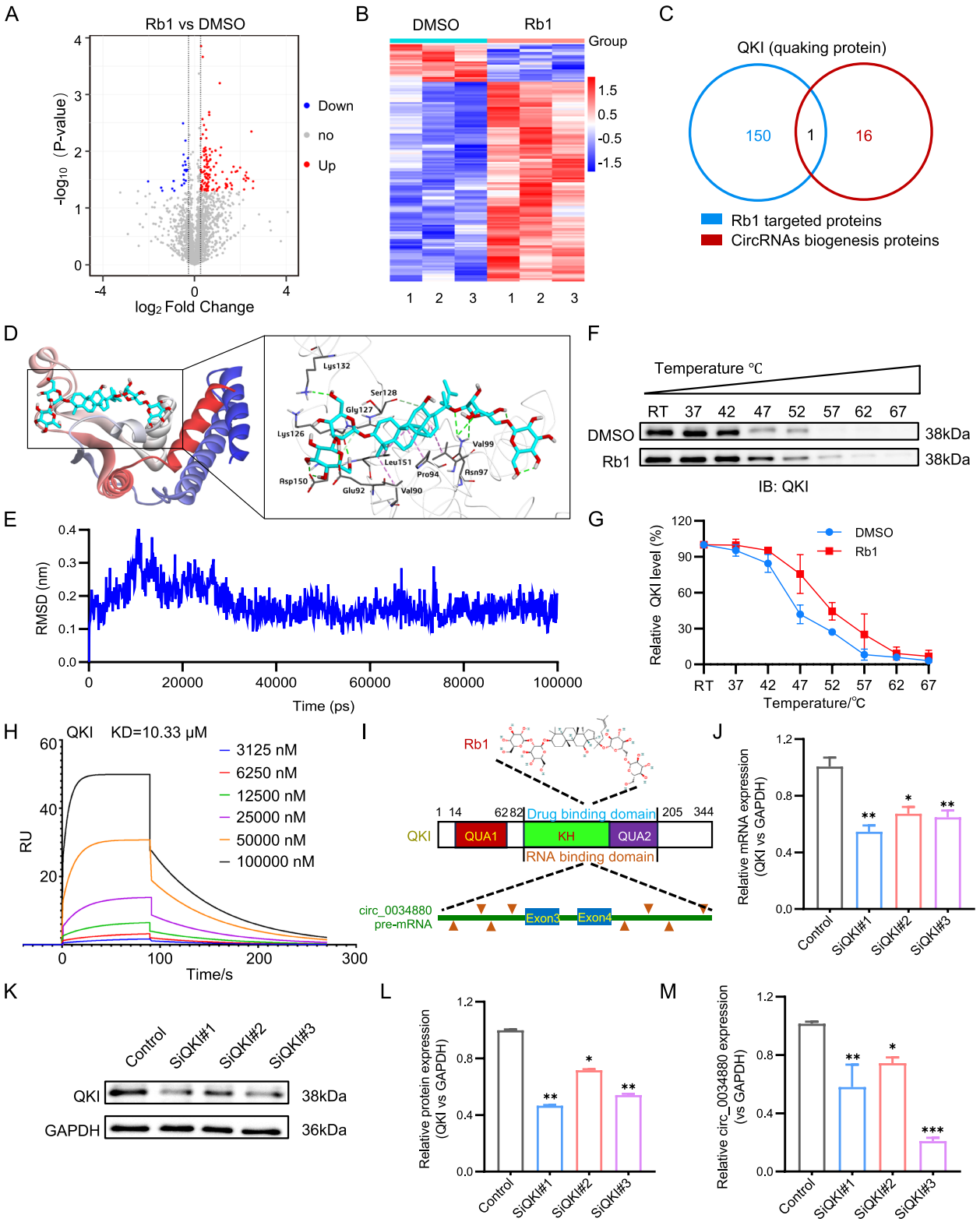

Fig. 7 (See legend on previous page.)

under the premise of circ-0034880 silencing, $CD206^+$ pro-tumor TAMs demonstrated minimal change following Rb1-pretreated TEVs administration (Fig. 8H, K). Flow cytometry assays in freshly resected liver metastatic tissues confirmed these results (Fig. S23). Moreover, we investigated the effects of Rb1 on circ-0034880 and SPP1 expression in liver metastases. Rb1-pretreated TEVs administration significantly reduced circ-0034880 expression compared to the untreated group, similar to direct circ-0034880 silencing. Nevertheless, under the premise of circ-0034880 silencing, the expression of the corresponding circ-0034880 did not change more in response to Rb1-pretreated TEVs administration (Fig. 8I, L). Similarly, SPP1 expression was significantly downregulated in the Rb1-pretreated TEVs administration group, resembling the effect of direct circ-0034880 silencing. However, under the premise of circ-0034880 silencing, SPP1 expression in corresponding liver metastases was minimally affected by Rb1-pretreated TEVs administration (Fig. 8J, M).

In summary, this study uncovers a novel mechanism by which circ-0034880-enriched TEVs promote the activation of $SPP1^{high}CD206^+$ pro-tumor TAMs, reshaping the liver tumor microenvironment. Additionally, we proposed Ginsenoside Rb1 as a potential alternative drug, which remodels the TME by directly targeting QKI protein and reducing the biogenesis of circ-0034880 to prevent CRLM (Fig. 8N).

Discussion

The TME plays a critical role in tumor metastasis, with EVs acting as crucial mediators in TME remodeling. EVs, akin to small transport aircraft, facilitate communication between tumors and the external microenvironment by exchanging lipids, proteins, mRNAs, and ncRNAs [38]. In the context of tumor diseases, EVs often spearhead the creation of a conducive microenvironment for tumor cells colonization and secondary growth post-metastasis [39]. In this study, we present clinical and experimental evidence supporting the role of circRNAs-enriched TEVs in CRLM.

Through database mining and validation in clinical samples, we identified circ-0034880-enriched TEVs as a potential marker for the diagnosis of CRLM. Subsequent *in vivo* experiments unequivocally confirmed the promoting effect of circ-0034880-enriched TEVs on CRLM, highlighting the crucial role of circ-0034880 in CRLM formation. These findings prompted us to investigate the mechanisms underlying the influence of circ-0034880-enriched TEVs on CRLM.

Previous studies have underscored the significance of TEVs in TME remodeling and distant tumor metastasis. For instance, our prior research revealed how ITGBL1-enriched TEVs remodel the TME by affecting cancer-associated fibroblasts (CAFs), thereby impacting distant tumor metastasis and growth [40]. Additionally, Liu et al. demonstrated the role of TEVs-RNA in metastatic niche formation and organ-specific metastatic tropism by recruiting neutrophils [41]. Furthermore, TEVs contribute significantly to shaping the immunosuppressive niche before liver metastasis [42]. As anticipated, circ-0034880-enriched TEVs exerted varying degrees of influence on various immune cells, particularly macrophages and fibroblasts. Notably, silencing circ-0034880 in tumor cells significantly reduced the activation of $CD206^+$ pro-tumor macrophages, suggesting that this activation pathway may be pivotal for circ-0034880-enriched TEVs to remodel the TME in liver tissues.

To substantiate this hypothesis, we conducted experiments using tissue samples from a mouse experimental liver metastasis model and clinical CRC liver metastases. Pathological analysis confirmed a positive correlation between high circ-0034880 expression and $CD206^+$

(See figure on next page.)

Fig. 8 Rb1 administration inhibits CRLM via impeding circ-0034880-enriched TEVs mediated activation of $SPP1^{high}CD206^+$ pro-tumor TAMs. **A** Flow chart of Rb1 intervention in mice model of experimental liver metastasis. **B**, **C** Luciferase-based bioluminescence imaging on experimental liver metastasis of the indicated mice treated without EVs or with EVs derived from circ-0034880-enriched MC38 cells, or circ-0034880-silenced MC38 cells, or Rb1. $n = 6$ for each group. Representative bioluminescent images of mice in indicated groups were shown in Fig. 8B, and the quantification data (fluorescence intensity) was presented in Fig. 8C. **D**, **E**, **F**, **G** Photograph and HE staining to observe the effect of Rb1 on liver metastasis of mice colon cancer. Scale bar, 2 mm (up), 500 μm (down). $n = 6$ for each group. Representative liver tissues images of mice in indicated groups were shown in Fig. 8D, and the quantification data (liver/body weight, %) was presented in Fig. 8F. Representative HE staining pictures of liver tissue sections from indicated mice were shown in Fig. 8E (up and middle). In addition, the representative immunohistochemical results using anti-CK20 and anti-glypican-3 (GPC-3) antibody were also shown in Fig. 8E to indicate that the metastatic origin of tumor in liver tissues are from colon tissues (down). The quantification data (tumor burden, %) for HE staining results was presented in Fig. 8G. Scale bar, 2 mm (up), 500 μm (middle), 40 μm (down). **H** Immunofluorescence analysis of TAMs in the liver metastatic tissues from above Rb1 intervene model. Scale bar, 50 μm. **I** FISH assay of circ-0034880 in the liver metastatic tissues from above Rb1 intervene model. Scale bar, 25 μm. **J** Immunofluorescence analysis of SPP1 in the liver metastatic tissues from above Rb1 intervene model. Scale bar, 20 μm. **K**, **L**, **M** The quantitative assay for Fig. 8H, I, J. **N** A schematic mechanism underlying interactions between primary CRC cells and macrophages in distant liver organs. All results were shown as mean ± SD. Student's t-test was used to analyze the data. *, $P < 0.05$; **, $P < 0.01$

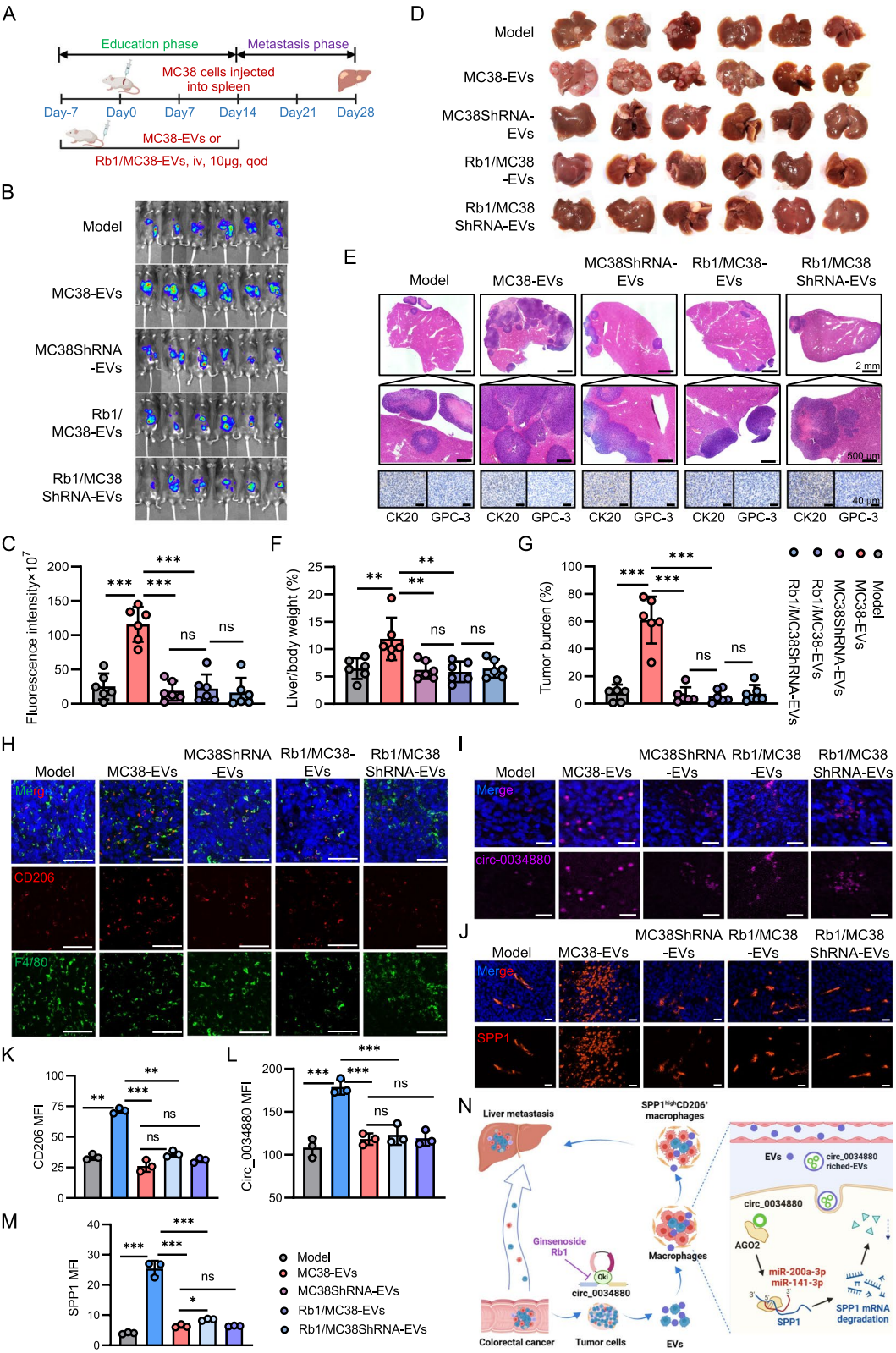

Fig. 8 (See legend on previous page.)

pro-tumor TAMs infiltration in mouse and human liver metastases. $CD206^+$ pro-tumor TAMs have been linked to tumor metastasis and growth [43]. Further *in vitro* experiments demonstrated that circ-0034880-enriched TEVs promoted tumor cells migration by upregulating the activation of $CD206^+$ pro-tumor macrophages. Through transcriptome analysis and related *in vitro* experiments, we identified SPP1 as a key mediator of circ-0034880-enriched TEVs in promoting the activation of $CD206^+$ pro-tumor macrophages. SPP1, abundant in various tumors, acts as a macrophage chemoattractant, essential for macrophage infiltration and pro-tumor activity maintenance [33]. We confirmed that circ-0034880-enriched TEVs facilitated the upregulation of SPP1 expression in macrophages, and the high expression of circ-0034880 positively correlated with SPP1 expression and $CD206^+$ pro-tumor TAM activation using mouse liver metastatic tissues and clinical metastatic tissues. Further mechanistic studies suggested that circ-0034880 serve as a sponge for miR-200a-3p and miR-141-3p, thereby increasing SPP1 expression by protecting it from degradation.

In the realm of anti-tumor metastasis research, various components of the TME, including CAFs, tumor-associated neutrophils (TANs), TAMs, myeloid-derived suppressor cells (MDSCs), regulatory T cells (Tregs), and EVs, have emerged as potential therapeutic targets. For instance, therapies targeting TANs and TAMs to reverse their tumor-promoting phenotype are under clinical investigation [44]. Inhibition of PMN-MDSCs ferroptosis and subsequent release of oxygenated lipids can reverse the immunosuppressive TME, rendering tumors more susceptible to immunotherapies [45]. Moreover, inhibiting EVs secretion can restore intracellular iron concentration, enhancing ferroptosis-based cancer therapy and immunotherapy [46]. Ginsenoside Rg3 exhibits high capture efficiency of circulating tumor cells (CTCs) and inhibits PMN formation, thereby inhibiting tumor lung metastasis by reversing the immune suppression microenvironment [47].

Currently, multiple therapy strategies including surgery, radiation therapy, ablation therapy, systemic therapy, anti-angiogenesis therapy, and immunotherapy are applied in clinic for patients with CRLM [48]. Furthermore, combined treatment and multidisciplinary cooperation have been established to reduce the mortality of CRLM patients. However, the prognosis for CRLM patients remains poor [49]. Therefore, it is very necessary to seek new methods to improve the existing therapy strategies for CRLM. Liang et al. demonstrated that inhibition of Cyclin-dependent kinase 8 (CDK8) significantly reduced the liver metastases of mouse and human colon cancer cells [50], suggesting that CDK8-targeting drugs might be a potential method for the treatment of CRLM. Shen et al. reported that anti-hypertensive drugs targeting the renin-angiotensin system (anti-RAS) in combination with bevacizumab could significantly improve the anti-angiogenic efficacy in CRLM [51]. In our study, we provide initial evidence that the natural product Ginsenoside Rb1, derived from Panax Ginsenoside, can inhibit CRLM by blocking the activation of $SPP1^{high}CD206^+$ pro-tumor macrophages. Rb1 achieves this by directly binding to the QKI protein, reducing circ-0034880 biogenesis and SPP1 expression, thereby suppressing PMN formation and inhibiting CRLM. In recent years, Ginsenoside Rb1 has been mainly reported to exert therapeutic roles in ischemic stroke [52], myocardial ischemia/reperfusion injury [53, 54], rheumatoid arthritis [55]. However, there are few high-quality reports on the therapeutic effects of Ginsenoside Rb1 in oncologic fields including CRC. From the perspective of regulating the TME, especially in inhibiting the biogenesis of circ-0034880 and generation of extracellular vesicles, our study reveals for the first time the special role of Ginsenoside Rb1 in the field of tumor prevention and treatment, laying a solid foundation for future clinical drug translation. Additionally, our supplementary data suggest that the promoting function of TEVs on CRLM can be attenuated by macrophage elimination (Fig. S24A, B).

Conclusion

In sum, this study elucidates the role of circ-0034880-enriched TEVs in promoting CRLM by enhancing the activation of $SPP1^{high}CD206^+$ pro-tumor macrophages, thereby reshaping the liver microenvironment to support PMN formation. Importantly, our mechanism insights led to the identification of Ginsenoside Rb1 as a potential therapeutic agent. Rb1 remodels the TME by directly targeting the QKI protein, thereby reducing circ-0034880 biogenesis and suppressing the activation of $SPP1^{high}CD206^+$ pro-tumor macrophages, ultimately inhibiting CRLM. These findings offer novel therapeutic avenues for combating colorectal cancer metastasis by targeting TME remodeling processes.

Abbreviations

CRC	Colorectal cancer
PMN	Pre-metastatic niche
CRLM	CRC liver metastasis
TME	Tumor microenvironment
EVs	Extracellular vesicles
TEVs	Tumor-derived EVs
MDSCs	Myeloid-derived suppressor cells
miRNAs	MicroRNAs
lncRNAs	Long noncoding RNAs
circRNAs	Circular RNAs
AGO2	Argonaute 2
SPP1	Secreted phosphoprotein 1
QKI	Splicing factor quaking protein
BMDMs	Bone marrow-derived macrophages

TAMs	Tumor-associated macrophages
CAFs	Cancer-associated fibroblasts
TANs	Tumor-associated neutrophils
Tregs	Regulatory T cells
CEL	Clodronate liposome
mRNAs	Messenger RNAs
ncRNAs	Noncoding RNAs
CTCs	Circulating tumor cells
GLUT1	Glucose transporter 1
NCBI	National Center for Biotechnology Information
ATCC	American Type Culture Collection
qPCR	Quantitative real-time PCR
FISH	Fluorescence in situ hybridization
DARTS	Drug affinity responsive target stability
CETSA	Cellular thermal shift assay

Supplementary Information

The online version contains supplementary material available at https://doi.org/10.1186/s12943-024-02086-9.

Supplementary Material 1.

Supplementary Material 2.

Supplementary Material 3.

Supplementary Material 4.

Acknowledgements
We thank Yongqi Chen from Department of Pathology, Shuguang Hospital, Shanghai University of Traditional Chinese Medicine for providing us with support for immunohistochemical staining experiments. We thank Sizhi Paul Gao from Memorial Sloan Kettering Cancer Center for providing us with support for language polishing.

Authors' contributions
QJ and JZ conceived and designed the study. QJ, HSL, GBG, LY and QS supervised the project. QJ, JZ, QS and HZL conducted the bioinformatics analysis of RNA sequencing and clinical data analysis. JZ, HZL, YZP, LL and WQR conducted the isolation and characterization of EVs. QJ, JZ and YZP performed the immunofluorescence analysis. JZ, HZL, YCH, YZP, ZYW and JS performed all the animal studies and pathology analysis. YCH, YZP and LL performed qPCR measurement. JZ, HZL, YCH, YZP, LL, WQR and XDL conducted plasmids construction, cell transfection and western blot analysis. QJ, JZ, LY, QS, HZL, HRZ, YQS, XYH and GHZ performed drug targets analysis and statistical analysis. QJ, HSL, GBG, LY, QS and JZ performed overall data interpretation and wrote the paper. All authors reviewed the manuscript.

Funding
This work was supported by grants from National Natural Science Foundation of China (82274297, 82074225, 82030118, 82274257, 82004136, 82374188, U23A20516), the Organizational Key Research and Development Program of Shanghai University of Traditional Chinese Medicine (2023YZZ02), Postdoctoral Research Foundation of China (2022M722159), Natural Science Foundation of Zhejiang Province (LQ23H290003), Natural Science Foundation of Ningbo (2023J404).

Availability of data and materials
The datasets used and/or analyzed during the current study are available from the corresponding author on reasonable request.

Data availability
No datasets were generated or analysed during the current study.

Declarations

Ethics approval and consent to participate
This study was approved by the Ethics Committee at Shuguang Hospital, Shanghai University of Traditional Chinese Medicine.

Consent for publication
All authors have agreed with publishing this manuscript.

Competing interests
The authors declare no competing interests.

Author details
[1]Department of Medical Oncology & Cancer Institute of Integrative Medicine, Shuguang Hospital, Shanghai University of Traditional Chinese Medicine, Shanghai 201203, China. [2]Liver Disease Department of Integrative Medicine, Ningbo No. 2 Hospital, Ningbo, Zhejiang 315010, China. [3]Department of Medical Oncology, Suzhou TCM Hospital Affiliated to Nanjing University of Chinese Medicine, Jiangsu 215007, China. [4]Department of Pathology, Shuguang Hospital, Shanghai University of Traditional Chinese Medicine, Shanghai 201203, China. [5]Department of Peripheral Vascular Disease, Shuguang Hospital, Shanghai University of Traditional Chinese Medicine, Shanghai 201203, China. [6]Institute of Interdisciplinary Integrative Medicine Research, Shanghai University of Traditional Chinese Medicine, Shanghai 201203, China. [7]Department of Oncology, Baoshan Hospital Affiliated to Shanghai University of Traditional Chinese Medicine, Shanghai 201203, China.

Received: 12 April 2024 Accepted: 13 August 2024
Published online: 20 August 2024

References

1. Sung H, Ferlay J, Siegel RL, et al. Global Cancer Statistics 2020: GLOBOCAN Estimates of Incidence and Mortality Worldwide for 36 Cancers in 185 Countries. CA Cancer J Clin. 2021;71:209–49. https://doi.org/10.3322/caac.21660.
2. Siegel RL, Wagle NS, Cercek A, et al. Colorectal cancer statistics, 2023. CA Cancer J Clin. 2023;73:233–54. https://doi.org/10.3322/caac.21772.
3. Dekker E, Tanis PJ, Vleugels JLA, et al. Colorectal cancer. Lancet. 2019;394:1467–80. https://doi.org/10.1016/S0140-6736(19)32319-0.
4. Wille-Jørgensen P, Syk I, Smedh K, et al. Effect of More vs Less Frequent Follow-up Testing on Overall and Colorectal Cancer-Specific Mortality in Patients With Stage II or III Colorectal Cancer: The COLOFOL Randomized Clinical Trial. JAMA. 2018;319:2095–103. https://doi.org/10.1001/jama.2018.5623.
5. Fares J, Fares MY, Khachfe HH, et al. Molecular principles of metastasis: a hallmark of cancer revisited. Signal Transduct Target Ther. 2020;5:28. https://doi.org/10.1038/s41392-020-0134-x.
6. Wang X, Cheng H, Zhao J, et al. Long noncoding RNA DLGAP1-AS2 promotes tumorigenesis and metastasis by regulating the Trim21/ELOA/LHPP axis in colorectal cancer. Mol Cancer. 2022;21:210. https://doi.org/10.1186/s12943-022-01675-w.
7. Tey SK, Wong SWK, Chan JYT, et al. Patient pIgR-enriched extracellular vesicles drive cancer stemness, tumorigenesis and metastasis in hepatocellular carcinoma. J Hepatol. 2022;76:883–95. https://doi.org/10.1016/j.jhep.2021.12.005.
8. Zhong Y, Yang L, Xiong F, et al. Long non-coding RNA AFAP1-AS1 accelerates lung cancer cells migration and invasion by interacting with SNIP1 to upregulate c-Myc. Signal Transduct Target Ther. 2021;6:240. https://doi.org/10.1038/s41392-021-00562-y.
9. Xiao Y, Yu D. Tumor microenvironment as a therapeutic target in cancer. Pharmacol Ther. 2020;221:107753. https://doi.org/10.1016/j.pharmthera.2020.107753.
10. Fong MY, Zhou W, Liu L, et al. Breast-cancer-secreted miR-122 reprograms glucose metabolism in premetastatic niche to promote metastasis. Nat Cell Biol. 2015;17:183–94. https://doi.org/10.1038/ncb3094.
11. Pan Z, Zhao R, Li B, et al. EWSR1-induced circNEIL3 promotes glioma progression and exosome-mediated macrophage immunosuppressive polarization via stabilizing IGF2BP3. Mol Cancer. 2022;21(1):16. https://doi.org/10.1186/s12943-021-01485-6.
12. Zhao S, Mi Y, Zheng B, et al. Highly-metastatic colorectal cancer cell released miR-181a-5p-rich extracellular vesicles promote liver metastasis by activating hepatic stellate cells and remodelling the tumour microenvironment. J Extracell Vesicles. 2022;11(1):e12186. https://doi.org/10.1002/jev2.12186.

13. Yang P, Qin H, Li Y, et al. CD36-mediated metabolic crosstalk between tumor cells and macrophages affects liver metastasis. Nat Commun. 2022;13(1):5782. https://doi.org/10.1038/s41467-022-33349-y.
14. Shi Q, Shen Q, Liu Y, et al. Increased glucose metabolism in TAMs fuels O-GlcNAcylation of lysosomal Cathepsin B to promote cancer metastasis and chemoresistance. Cancer Cell. 2022;40(10):1207-1222.e10. https://doi.org/10.1016/j.ccell.2022.08.012.
15. Lai H, Li Y, Zhang H, et al. exoRBase 2.0: an atlas of mRNA, lncRNA and circRNA in extracellular vesicles from human biofluids. Nucleic Acids Res. 2022;50:D118–28. https://doi.org/10.1093/nar/gkab1085.
16. Glažar P, Papavasileiou P, Rajewsky N. circBase: a database for circular RNAs. RNA. 2014;20:1666–1170. https://doi.org/10.1261/rna.043687.113.
17. Lötvall J, Hill AF, Hochberg F, et al. Minimal experimental requirements for definition of extracellular vesicles and their functions: a position statement from the International Society for Extracellular Vesicles. J Extracell Vesicles. 2014;3:26913. https://doi.org/10.3402/jev.v3.26913.
18. Witwer KW, Buzás EI, Bemis LT, et al. Standardization of sample collection, isolation and analysis methods in extracellular vesicle research. J Extracell Vesicles. 2013;2:20360. https://doi.org/10.3402/jev.v2i0.20360.
19. Zhang M, Pan X, Fujiwara K, et al. Pancreatic cancer cells render tumor-associated macrophages metabolically reprogrammed by a GARP and DNA methylation-mediated mechanism. Signal Transduct Target Ther. 2021;6:366. https://doi.org/10.1038/s41392-021-00769-z.
20. Lomenick B, Hao R, Jonai N, et al. Target identification using drug affinity responsive target stability (DARTS). Proc Natl Acad Sci U S A. 2009;106:21984–9. https://doi.org/10.1073/pnas.0910040106.
21. Neubert H, Bonnert TP, Rumpel K, et al. Label-free detection of differential protein expression by LC/MALDI mass spectrometry. J Proteome Res. 2008;7:2270–9. https://doi.org/10.1021/pr700705u.
22. Jumper J, Evans R, Pritzel A, et al. Highly accurate protein structure prediction with AlphaFold. Nature. 2021;596:583–9. https://doi.org/10.1038/s41586-021-03819-2.
23. Wang S, Xie J, Pei J, et al. CavityPlus 2022 Update: An Integrated Platform for Comprehensive Protein Cavity Detection and Property Analyses with User-friendly Tools and Cavity Databases. J Mol Biol. 2023;435:168141. https://doi.org/10.1016/j.jmb.2023.168141.
24. Eberhardt J, Santos-Martins D, Tillack AF, et al. AutoDock Vina 1.2.0: New Docking Methods, Expanded Force Field, and Python Bindings. J Chem Inf Model. 2021;61:3891–8. https://doi.org/10.1021/acs.jcim.1c00203.
25. Liu M, Tong Z, Ding C, et al. Transcription factor c-Maf is a checkpoint that programs macrophages in lung cancer. J Clin Invest. 2020;130:2081–96. https://doi.org/10.1172/JCI131335.
26. Chen P, Zuo H, Xiong H, et al. Gpr132 sensing of lactate mediates tumor-macrophage interplay to promote breast cancer metastasis. Proc Natl Acad Sci U S A. 2017;114:580–5. https://doi.org/10.1073/pnas.1614035114.
27. Wei C, Yang C, Wang S, et al. Crosstalk between cancer cells and tumor associated macrophages is required for mesenchymal circulating tumor cell-mediated colorectal cancer metastasis. Mol Cancer. 2019;18(1):64. https://doi.org/10.1186/s12943-019-0976-4.
28. Chen W, Zhou M, Guan B, et al. Tumour-associated macrophage-derived DOCK7-enriched extracellular vesicles drive tumour metastasis in colorectal cancer via the RAC1/ABCA1 axis. Clin Transl Med. 2024;14(2):e1591. https://doi.org/10.1002/ctm2.1591.
29. Xu C, Fan L, Lin Y, et al. Fusobacterium nucleatum promotes colorectal cancer metastasis through miR-1322/CCL20 axis and M2 polarization. Gut Microbes. 2021;13(1):1980347. https://doi.org/10.1080/19490976.2021.1980347.
30. Pitarresi JR, Norgard RJ, Chiarella AM, et al. PTHrP Drives Pancreatic Cancer Growth and Metastasis and Reveals a New Therapeutic Vulnerability. Cancer Discov. 2021;11:1774–91. https://doi.org/10.1158/2159-8290.CD-20-1098.
31. Qi J, Sun H, Zhang Y, et al. Single-cell and spatial analysis reveal interaction of FAP^+ fibroblasts and $SPP1^+$ macrophages in colorectal cancer. Nat Commun. 2022;13:1742. https://doi.org/10.1038/s41467-022-29366-6.
32. Liu Y, Zhang Q, Xing B, et al. Immune phenotypic linkage between colorectal cancer and liver metastasis. Cancer Cell. 2022;40:424-437.e5. https://doi.org/10.1016/j.ccell.2022.02.013.
33. Wei J, Marisetty A, Schrand B, et al. Osteopontin mediates glioblastoma-associated macrophage infiltration and is a potential therapeutic target. J Clin Invest. 2019;129:137–49. https://doi.org/10.1172/JCI121266.
34. Chen P, Zhao D, Li J, et al. Symbiotic Macrophage-Glioma Cell Interactions Reveal Synthetic Lethality in PTEN-Null Glioma. Cancer Cell. 2019;35:868-884.e6. https://doi.org/10.1016/j.ccell.2019.05.003.
35. van der Veer EP, de Bruin RG, Kraaijeveld AO, et al. Quaking, an RNA-binding protein, is a critical regulator of vascular smooth muscle cell phenotype. Circ Res. 2013;113:1065–75. https://doi.org/10.1161/CIRCRESAHA.113.301302.
36. Liang D, Wilusz JE. Short intronic repeat sequences facilitate circular RNA production. Genes Dev. 2014;28:2233–47. https://doi.org/10.1101/gad.251926.114.
37. Beuck C, Qu S, Fagg WS, et al. Structural analysis of the quaking homodimerization interface. J Mol Biol. 2012;423:766–81. https://doi.org/10.1016/j.jmb.2012.08.027.
38. Zhang DX, Vu LT, Ismail NN, et al. Landscape of extracellular vesicles in the tumour microenvironment: Interactions with stromal cells and with non-cell components, and impacts on metabolic reprogramming, horizontal transfer of neoplastic traits, and the emergence of therapeutic resistance. Semin Cancer Biol. 2021;74:24–44. https://doi.org/10.1016/j.semcancer.2021.01.007.
39. Becker A, Thakur BK, Weiss JM, et al. Extracellular Vesicles in Cancer: Cell-to-Cell Mediators of Metastasis. Cancer Cell. 2016;30:836–48. https://doi.org/10.1016/j.ccell.2016.10.009.
40. Ji Q, Zhou L, Sui H, et al. Primary tumors release ITGBL1-rich extracellular vesicles to promote distal metastatic tumor growth through fibroblast-niche formation. Nat Commun. 2020;11:1211. https://doi.org/10.1038/s41467-020-14869-x.
41. Liu Y, Gu Y, Han Y, et al. Tumor Exosomal RNAs Promote Lung Premetastatic Niche Formation by Activating Alveolar Epithelial TLR3 to Recruit Neutrophils. Cancer Cell. 2016;30:243–56. https://doi.org/10.1016/j.ccell.2016.06.021.
42. Yang X, Zhang Y, Zhang Y, et al. Colorectal cancer-derived extracellular vesicles induce liver premetastatic immunosuppressive niche formation to promote tumor early liver metastasis. Signal Transduct Target Ther. 2023;8:102. https://doi.org/10.1038/s41392-023-01384-w.
43. Mantovani A, Allavena P, Marchesi F, et al. Macrophages as tools and targets in cancer therapy. Nat Rev Drug Discov. 2022;21:799–820. https://doi.org/10.1038/s41573-022-00520-5.
44. Que H, Fu Q, Lan T, et al. Tumor-associated neutrophils and neutrophil-targeted cancer therapies. Biochim Biophys Acta Rev Cancer. 2022;1877:188762. https://doi.org/10.1016/j.bbcan.2022.188762.
45. Kim R, Hashimoto A, Markosyan N, et al. Ferroptosis of tumour neutrophils causes immune suppression in cancer. Nature. 2022;612:338–46. https://doi.org/10.1038/s41586-022-05443-0.
46. Wang Y, Chen Q, Song H, et al. A Triple Therapeutic Strategy with Antiexosomal Iron Efflux for Enhanced Ferroptosis Therapy and Immunotherapy. Small. 2022;18:e2201704. https://doi.org/10.1002/smll.202201704.
47. Xia J, Ma S, Zhu X, et al. Versatile ginsenoside Rg3 liposomes inhibit tumor metastasis by capturing circulating tumor cells and destroying metastatic niches. Sci Adv. 2022;8:eabj1262. https://doi.org/10.1126/sciadv.abj1262.
48. Zhou H, Liu Z, Wang Y, et al. Colorectal liver metastasis: molecular mechanism and interventional therapy. Signal Transduct Target Ther. 2022;7(1):70. https://doi.org/10.1038/s41392-022-00922-2.
49. Biller LH, Schrag D. Diagnosis and Treatment of Metastatic Colorectal Cancer: A Review. JAMA. 2021;325:669–85. https://doi.org/10.1001/jama.2021.0106.
50. Liang J, Chen M, Hughes D, et al. CDK8 Selectively Promotes the Growth of Colon Cancer Metastases in the Liver by Regulating Gene Expression of TIMP3 and Matrix Metalloproteinases. Cancer Res. 2018;78:6594–606. https://doi.org/10.1158/0008-5472.CAN-18-1583.
51. Shen Y, Wang X, Lu J, et al. Reduction of Liver Metastasis Stiffness Improves Response to Bevacizumab in Metastatic Colorectal Cancer. Cancer Cell. 2020;37:800-817.e7. https://doi.org/10.1016/j.ccell.2020.05.005.
52. Ni XC, Wang HF, Cai YY, et al. Ginsenoside Rb1 inhibits astrocyte activation and promotes transfer of astrocytic mitochondria to neurons against ischemic stroke. Redox Biol. 2022;54:102363. https://doi.org/10.1016/j.redox.2022.102363.

53. Jiang L, Yin X, Chen YH, et al. Proteomic analysis reveals ginsenoside Rb1 attenuates myocardial ischemia/reperfusion injury through inhibiting ROS production from mitochondrial complex I. Theranostics. 2021;11(4):1703–20. https://doi.org/10.7150/thno.43895.
54. Wang J, Qiao L, Li Y, et al. Ginsenoside Rb1 attenuates intestinal ischemia-reperfusion- induced liver injury by inhibiting NF-kappaB activation. Exp Mol Med. 2008;40(6):686–98. https://doi.org/10.3858/emm.2008.40.6.686.
55. Li S, Li JJ, Zhao YY, et al. Supramolecular Integration of Multifunctional Nanomaterial by Mannose-Decorated Azocalixarene with Ginsenoside Rb1 for Synergistic Therapy of Rheumatoid Arthritis. ACS Nano. 2023;17(24):25468–82. https://doi.org/10.1021/acsnano.3c09140.

Publisher's Note